PONTIFÍCIA UNIVERSIDADE CATÓLICA
DO RIO DE JANEIRO

Oliver Eugenio Everett Espino

Study of the influence of the support in the CO_2 methanation reaction using Ni based catalysts

Tese de Doutorado

Thesis presented to the Programa de Pós-Graduação em Engenharia de Materiais e de Processos Químicos e Metalúrgicos of PUC-Rio in partial fulfillment of the requirements for the degree of Doutor em Engenharia de Materiais e de Processos Químicos e Metalúrgicos.

Advisor: Prof. Roberto Ribeiro de Avillez
Co-Advisor: Drª. Lucia Gorenstin Appel

Rio de Janeiro

September of 2019

PONTIFÍCIA UNIVERSIDADE CATÓLICA
DO RIO DE JANEIRO

Oliver Eugenio Everett Espino

Study of the influence of the support in the CO$_2$ methanation reaction using Ni based catalysts

Thesis presented to the Programa de Pós-Graduação em Engenharia de Materiais e de Processos Químicos e Metalúrgicos of PUC-Rio in partial fulfillment of the requirements for the degree of Doutor em Engenharia de Materiais e de Processos Químicos e Metalúrgicos Approved by the Examination Committee.

Prof. Roberto Ribeiro de Avillez
Advisor

Departamento de Engenharia Química e de Materiais – PUC-Rio

Drª. Lucia Gorenstin Appel
Co-Advisor
INT

Prof.ª Fatima Maria Zanon Zotin
UERJ

Prof.ª Amanda Lemette Teixeira Brandão
PUC-RIO

Prof. Rodrigo Fernandes Magalhães de Souza
PUC-RIO

Dr. Alexandre Barros Gaspar
INT

Rio de Janeiro , September 27th, 2019

Oliver Eugenio Everett Espino

He graduated in Chemical Engineering at Universidad Nacional Autónoma de Honduras in 2010. He holds a master degree in Chemistry from PUC-Rio (2015) with emphasis in catalysis. He Worked as a laboratory instructor at the Physics Department of UNAH (2007-2013). He worked at the National Institute of Technology of Brazil (2015-2019) at the catalysis department.

I dedicate this work primarily to

God and my family.

Acknowledgments

Abstract

Espino, Oliver Eugenio Everett; De Avillez, Roberto Ribeiro (Advisor); Appel, Lucia Gorenstin (Co-Advisor). **Study of the influence of the support in the CO_2 methanation reaction using Ni based catalysts.** Rio de Janeiro, 2019. 98p. Tese de Doutorado – Departamento de Engenharia Química e de Materiais, Pontifícia Universidade Católica do Rio de Janeiro.

The Ni/ZrO_2, Ni/$CaZrO_2$, Ni/SiO_2 and Ni/Mg(Al)O catalysts were employed in the CO_2 methanation. The catalysts were characterized by XPS (reduced *in situ* and passivated), XRD (reduced *in situ* and passivated along with Rietveld refinement), EPR, TPSR of CO_2 + H_2 and CO + H_2, cyclohexane dehydrogenation model reaction, CO_2-TPD and chemical analysis. The metallic area of all of these catalysts was prepared to be similar among them in order to investigate the role of the support during the methanation of CO_2. The behaviors of these catalysts in the CO_2 methanation were analyzed employing a conventional catalytic test. The Ni/ZrO_2 catalyst exhibited the highest activity and selectivity toward the methanation of CO_2 against Ni/Mg(Al)O and Ni/SiO_2. Oxygen vacancies are suggested to be responsible for the excellent performance of the Ni/ZrO_2 catalyst. Based on the above, Ca was added to the Ni/ZrO_2 catalyst, the metallic area did not change whereas the CO_2 consumption rate almost tripled. The XRD, XPS and EPR analyses showed that mainly Ca^{+2} but also some Ni^{2+} are on the ZrO_2 lattice surface of the Ni/$CaZrO_2$ catalyst. These cations form oxygen vacancies and unsaturated coordination sites (cus) pairs, which are strong basic and acid sites pairs, respectively. In short, increasing the concentration of these pairs by adding Ca to Ni/ZrO_2, not only does the amount of CO_2 adsorbed increase, but also the number of active sites of the rate limiting step, which is enhanced leading to an increase of the Zr based catalyst activity in the CO_2 methanation.

Keywords

Methanation; carbon dioxide; carbon monoxide; oxygen vacancies; cus.

Resumo

Espino, Oliver Eugenio Everett; De Avillez, Roberto Ribeiro; Appel, Lucia Gorenstin. **Estudo da influência do suporte na reação de metanação de CO$_2$ utilizando catalisadores à base de Ni.** Rio de Janeiro, 2019. 98p. Tese de Doutorado – Departamento de Engenharia Química e de Materiais, Pontifícia Universidade Católica do Rio de Janeiro.

Os catalisadores de Ni/ZrO$_2$, Ni/CaZrO$_2$, Ni/SiO$_2$ e Ni/Mg(Al)O foram empregados na reação de metanação do CO$_2$. Os catalisadores foram caracterizados por XPS, XRD e os dados foram tratados pelo método de refinamento de Rietveld, EPR, TPR, TPSR de CO$_2$ + H$_2$ e CO + H$_2$, reação modelo de desidrogenação do ciclohexano, TPD de CO$_2$, análise química (FRX) e área superficial (BET). Com o objetivo de investigar o papel do suporte durante a metanação do CO$_2$, os catalisadores foram preparados de modo a se obter a mesma área metálica de níquel. Os comportamentos catalíticos desses catalisadores na metanação do CO$_2$ foram avaliados através de testes catalíticos convencionais e da taxa da reação. O catalisador Ni/ZrO$_2$ apresentou maior atividade e seletividade para a metanação de CO$_2$ quando comparado com os catalisadores de Ni/Mg(Al)O e Ni/SiO$_2$. Sugere-se que as vacâncias de oxigênio sejam responsáveis pelo melhor desempenho do catalisador Ni/ZrO$_2$. Ca foi adicionado ao catalisador Ni/ZrO$_2$ com o objetivo de aumentar as vacâncias oxigênio. A área da superfície metálica do catalisador contendo Ca não se alterou, enquanto a taxa de consumo de CO$_2$ quase triplicou. As análises de DRX, XPS e EPR mostraram que principalmente Ca^{+2}, mas também ions de Ni^{2+} estão na superfície da rede de ZrO$_2$ no catalisador Ni/CaZrO$_2$. Esses cátions formam vacâncias de oxigênio e pares de sítios de coordenação insaturados (cus), os quais são pares de sítios básicos e ácidos fortes. Em resumo, os dados obtidos indicaram que aumentando a concentração destes pares de sítios pela adição de Ca no Ni/ZrO$_2$, não só aumenta a quantidade de CO$_2$ adsorvido, mas também aumenta o número de sitios ativos da etapa limitante da reação.

Palavras-Chave

Metanação; dióxido de carbono; monóxido de carbono; vacâncias de oxigênio; cus.

Summary

List of figures

List of tables

List of abbreviations

Abbreviation	Explanation
RWGS	Reverse water gas shift reaction
SNG	Synthetic natural gas
MSN	Mesoporous SiO_2 nanoparticles
GHSV	Gas hourly space velocity
DRIFTS	Diffuse reflectance infrared fourier transform spectroscopy
RDS	Rate-determining step
TCD	Thermal conductivity detector
WGSR	Water gas shift reaction
DFT	Density functional theory
K	Equilibrium constant
PCO	Partial pressure of CO
PH_2	Partial pressure of H_2
PH_2O	Partial pressure of H_2O
a_c	Carbon activity
ABEEólica	Associação Brasileira de Energia Eólica

1.
Introduction

The use of fossil fuels has enabled the rapid and unprecedented development of human society. However, the consumption of these resources is accompanied by large amounts of CO_2 emissions causing global environmental changes. Chemical recycling of CO_2 in fuels, mainly methane, offers a powerful alternative to address issues of fuel depletion and climate change [1].

Renewable sources such as wind and solar power are gaining special interest, due to concerns to replace conventional fossil fuels. One of the main problems of these renewable energy sources is associated with intermittence, since wind energy is only available when the wind blows and solar energy only available during the day. CO_2 methanation process offers an applicable solution to this problem, by producing methane. Electricity from a renewable resource, which is in excess can be used to produce hydrogen by water electrolysis, which would react with CO_2 captured from emission sources producing methane. Hence, this compound can be used directly as a fuel, indirectly as an energy source stored to generate electricity in a power plant or be injected into the existing natural gas grid [2]. The above concept will turn CO_2 from contaminant waste into a raw material of the methane production, offering an opportunity to reduce greenhouse gases effect and also providing an alternative to store electricity from renewable sources.

The CO_2 methanation reaction is shown in equation 1. This concept of using CO_2 to produce methane as fuel, is currently carried out on an industrial scale by the Audi Motor Company at the "E-gas" plant in Werlte, Germany [3].

$$CO_2(g) + 4H_2(g) \leftrightarrow CH_4(g) + 2H_2O(g) \quad \Delta H_{298K} = -164 \text{ kJ/mol} \quad (1)$$

Audi' plant uses renewable energy and carbon dioxide to make SNG (synthetic natural gas). SNG made at this plant is distributed compressed to a natural gas stations via Germany's natural gas network and powers some Audi's vehicles.

Figure 1 shows the scheme of the Audi's SNG plant, which has the capacity to convert 6 MW of power, from renewable electricity into H_2 and O_2 through water electrolysis. Then, the H_2 reacts with the CO_2 molecule in a methanation reactor to generate renewable synthetic methane. The CO_2 used in the plant is a waste byproduct from a nearby biogas plant. This plant produces about 1,000 metric tons of SNG each year. Clariant has supplied the methanation catalyst for this plant [4].
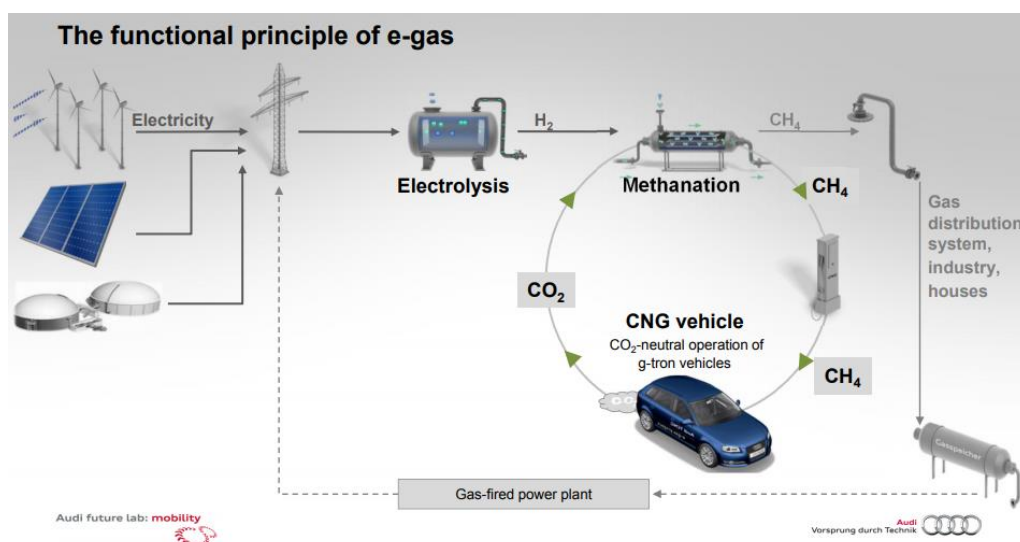
Figure 1. Audi's PTG scheme plant (adapted from CEDEC gas day [4]).

The essential issue of the methanation process is the design of the catalyst. An excellent catalyst used in the methanation of CO_2 should have high activity at low temperatures (200-500°C), since it is an exothermic reaction. In the past years, several catalysts have been investigated for the methanation process among which are the transition metals Ni, Fe, Co, Ru, Mo, dispersed on a metal oxide as support (Al_2O_3, SiO_2, TiO_2, ZrO_2, CeO_2 and others.) [5]. Two areas have been investigated recently:

1) The development of the catalyst for the methanation reaction, employing many different combinations of metal supported on metal oxide prepared by different methods.

2) Studies related to the reaction mechanism. Indeed, increasing the knowledge about the CO_2 methanation it will lead to the project of more active and selective catalysts.

Figure 2 presents the increasing interest in CO_2 methanation in the last two decades according to Scopus data base. It can be seen that from 2016 through 2018 publications have soared by up to 50 documents. This interest is motivated by the environmental issues as described above.
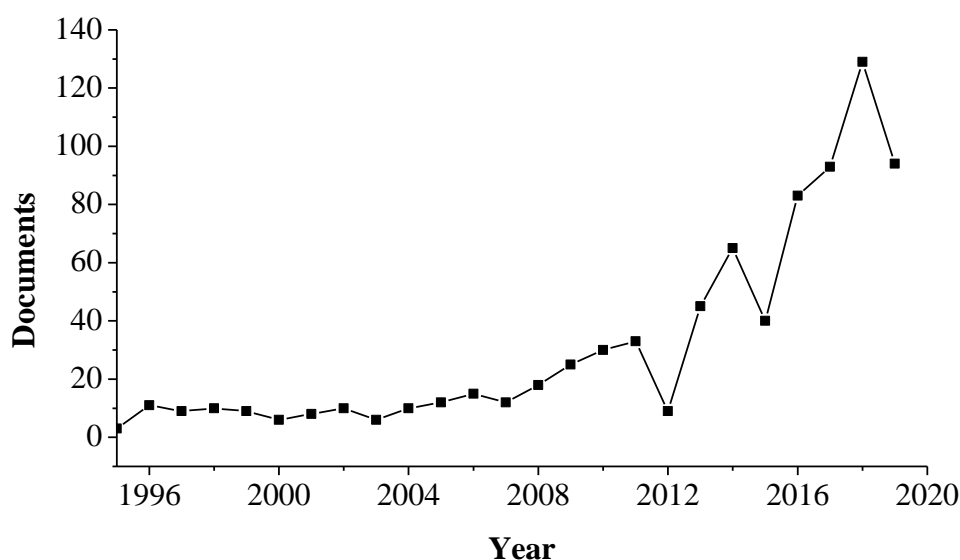
Figure 2. Publications related to CO_2 methanation per year (Calculated from Scopus data base). The keywords used in this search were: CO_2, methanation, catalyst.

Figure 3 displays the countries/regions with highest scientific production in the CO_2 methanation field, China leads the row with 170 documents followed by Germany and Japan with 79 and 75 documents each one, respectively.

16
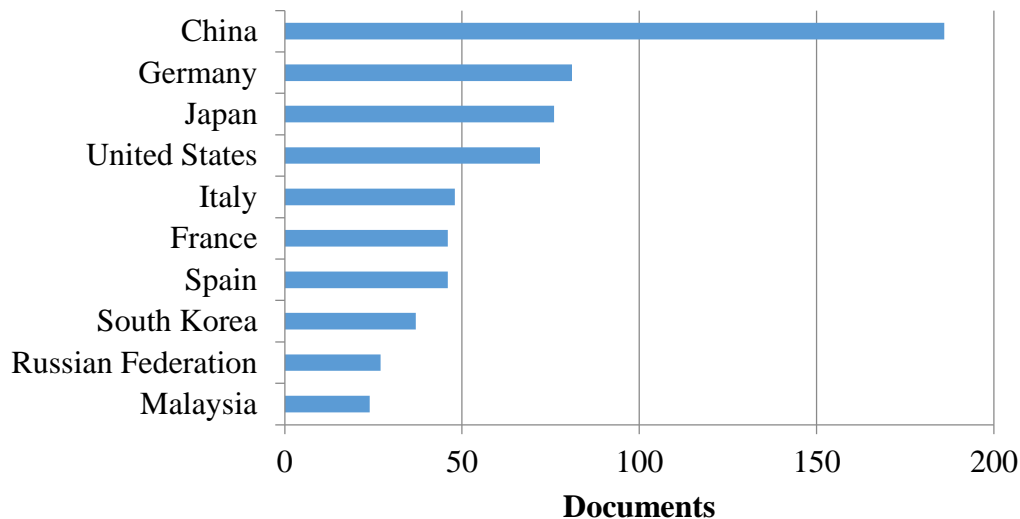
Figure 3. Countries with highest scientific production for CO_2 methanation (Adapted from Scopus data base).

Brazil is growing in the world ranking of installed capacity of wind energy. In 2017, it occupied the eighth position, according to a survey by the Global World Energy Council (GWEC) and released by the Brazilian Wind Energy Association (ABEEólica). The installed wind energy capacity grew 28.1%, reaching the mark of 12.8 gigawatts (GW) distributed among 500 generation parks, equivalent to 8.1% of all capacity in Brazil. According to Almeida and Azevedo [6] the wind installed capacity in Brazil registered until October 2018 was about 14.34 GW, enough to power 26 million homes. Federal government of Brazil expects an expansion of wind power installed capacity of 125% by 2026 [7].

In the case of solar energy, the jump was even more impressive: 4,470% in just one year. In early 2017, it was only 21 megawatts, which, at the turn of the year, were close to the first gigawatt. This number, however, should be seen with moderation: solar power continues in the eye of the national generation system, with only 0.6% of installed power in Brazil. This growth of renewable sources is accompanied by an interest in finding a way to store these energies, possibly visualized in the production of methane via CO_2/H_2 [8].

This work is devoted to the study of the influence of the support of the methanation reaction from CO_2/H_2 under stoichiometric conditions to evaluate and understand the catalytic performance of Ni/ZrO_2 catalysts in comparison with typical Ni/SiO_2, and $Ni/Mg(Al)O$ catalysts. Moreover, this work will also contribute for the description of the CO_2 methanation by describing the role of oxygen vacancies on the support of the catalyst. The innovation of this work is based on the creation of a Ni/ZrO_2 catalyst with a greater concentration of oxygen vacancies in order to enhance its activity during the CO_2 methanation reaction, as well as to contribute to description of the mechanism of the methanation of CO_2.

2.
Literature review

2.1.
Introduction

The conversion of carbon dioxide to methane is called the Sabatier process which is a highly researched reaction. Attributed to the french chemist Paul Sabatier, a pioneer in the catalytic hydrogenation processes, who discovered it in the 1910s [9]. The Sabatier reaction is as shown below (Equation 1):

$$CO_2(g) + 4H_2(g) \leftrightarrow CH_4(g) + 2H_2O(g) \qquad \Delta H_{298K} = -164 \text{ kJ/mol} \qquad (1)$$
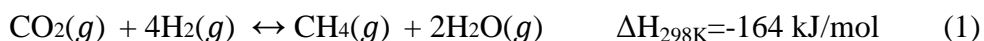
Sabatier reaction is a highly exothermic reaction, with an enthalpy of $\Delta H_{298K} = -164$ kJ/mol. Thus, high conversions (equilibrium) are achieved at low temperatures. It has a free Gibbs energy of $\Delta G_{298K} = -113.5$ kJ/mol, which makes the reaction feasible.

Even though the methanation of CO_2 seems to be a simple reaction, its mechanism is quite complicated. Two main reaction paths have been proposed in the literature. The first one refers to the conversion of CO_2 to CO involving the Reverse Water Gas Shift Reaction (RWGS), which produces CO and H_2O from CO_2 and H_2 as shown in equation 2. After that, CO is hydrogenated to methane.

$$CO_2(g) + H_2(g) \rightarrow CO(g) + H_2O(g) \qquad \Delta H_{298K} = -41 \text{ kJ/mol (RWGS)} \qquad (2)$$

The second path, according to Aldana et al. [2], refers to the hydrogenation of carbonates, formates and methoxy species from CO_2.

Methane can also be produced via CO methanation. The CO methanation process is a highly exothermic $\Delta H_{298K} = -206.1$ kJ/mol and thermodynamically favorable reaction. According to Bartholomew et al. [10], the reaction of CO and

H_2 over a nickel-based catalyst is less selective towards methane than is CO_2 methanation. High temperatures may cause severe sintering of catalyst, which emphasizes the importance for the improvement of methanation activity in the low temperature region [11]. Equation 3 describes the reaction:

$$CO(g) + 3H_2(g) \rightarrow CH_4(g) + H_2O(g) \quad \Delta H_{295K} = =-206.1 \text{ kJ/mol} \tag{3}$$

2.2.
Thermodynamics of CO_2 Methanation

Gao et al., [12] described how the temperature, pressure, H_2 / CO and H_2 / CO_2 ratios, and the addition of H_2O, O_2, CH_4, C_2H_4 in the feed gas modified the CO conversion CO_2 and CH_4 selectivities and the coke deposition. The experimental data obtained were generated from commercial Ni-based catalysts. The authors verified that, at low temperature, high pressure and high H_2 / CO or H_2 / CO_2 ratios promote the methanation reactions. The addition of steam into the feed gas prevents carbon deposition.

Indeed, the deposition of carbon might occur on the surface of the catalyst during the methanation reaction as shown in equation 4. This happens if carbon activity (a_c) in the gas is greater than 1, causing deactivation of the catalyst which is one of the major problems in the industry [10].

$$CO_{(g)} + H_{2(g)} \rightarrow C + H_2O_{(g)} \qquad \Delta H = =-131.3 \text{ kJ/mol} \tag{4}$$

$$a_c = \frac{K * PCO * PH_2}{PH_2O}$$

Data related to the formation of carbon can lead to the determination of the ideal operating conditions, also providing pieces of information related to how increase the life of the catalysts [13].

Methanation is a complex reaction, some minor secondary reactions may occur affecting the purity of the product. Table 1 lists the probable reactions involved in the methanation process. In addition to the usual reactions (R1 and R2), the methanation reaction of CO which generates CO_2 can also occur in a lower H_2 / CO ratio (R3). The WGSR (water gas shift reaction) can also occur by modifying the surface and the kinetics of the methanation reaction. On the other

hand, the conditions of high pressures favor the R1 and R2, since the molar number of the reagents is greater than for the products. Further, these reactions are exothermic, so lower temperatures will favor them [14].

The equilibrium constants of the eight reactions involved in the methanation process are calculated at different temperature as shown in Figure 4. Since all the reactions exhibits negative enthalpies, they are all favorable at low temperatures (<400 °C) due to their exothermic characteristics [12]. According to Le Châtelier principle, low temperature and high pressure are preferred for carbon monoxide and carbon dioxide methanation. Due to the latter explanation, an ideal catalyst for the methanation of CO_2 and CO must favor the reactions to achieve equilibrium at low temperatures.

Table 1. Reactions involved in methanation at 1 atm pressure (adapted from Gao et al. [17]).

Reaction no.	Reaction formula	$\Delta H_{298\,K}$ (kJ mol^{-1})	$\Delta G_{298\,K}$ (kJ mol^{-1})
R1	$CO + 3H_2 \leftrightarrow CH_4 + H_2O$	-206.1	-141.8
R2	$CO_2 + 4H_2 \leftrightarrow CH_4 + 2H_2O$	-165.0	-113.2
R3	$2CO + 2H_2 \leftrightarrow CH_4 + CO_2$	-247.3	-170.4
R4	$2CO \leftrightarrow C + CO_2$	-172.4	-119.7
R5	$CO + H_2O \leftrightarrow CO_2 + H_2$	-41.2	-28.6
R6	$2H_2 + C \leftrightarrow CH_4$	-74.8	-50.7
R7	$CO + H_2 \leftrightarrow C + H_2O$	-131.3	-91.1
R8	$CO_2 + 2H_2 \leftrightarrow C + 2H_2O$	-90.1	-62.5
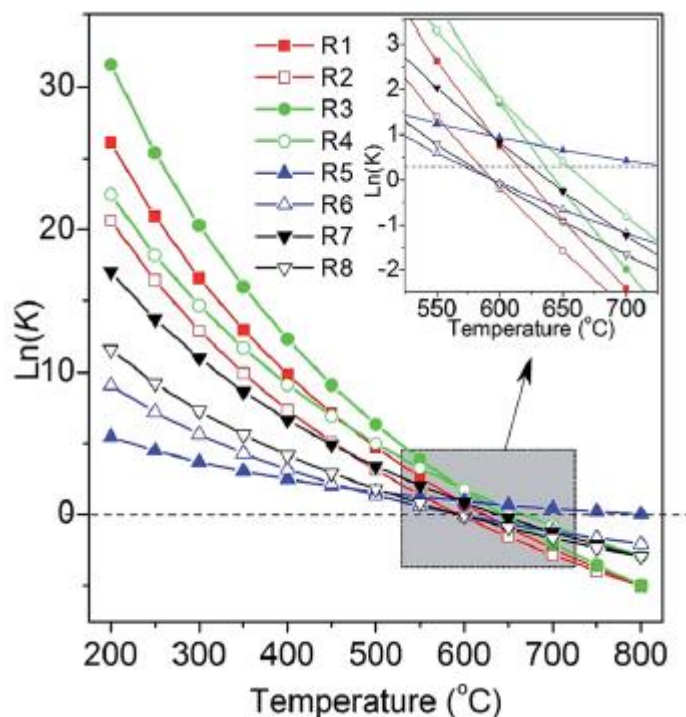
Figure 4. Representation of the equilibrium constant Ln(K) versus temperature for the reactions involved in the methanation process (extracted from Gao et al. [17].)

Figure 5 reveals that, at low temperatures, 200-250°C and atmospheric pressure, the main products of the methanation of CO_2 are CH_4 and H_2O. The selectivities are highly dependent on the temperature. Above 450°C the methane fraction starts to decrease, while the by-product CO starts to increase due to the RWGS. There is also an increase of CO_2 and H_2 that does not react [12,15]. The curves are calculated from the ideal gas phase using equilibrium thermodynamics [16].
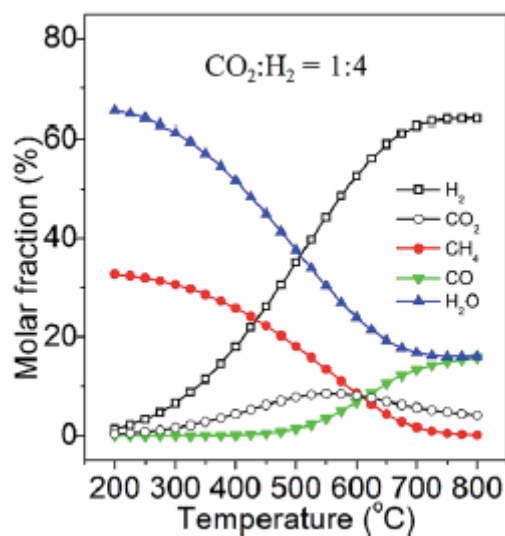
Figure 5. Methanation at equilibrium (0.1 MPa). Extracted from (Gao et al. [12]) .

Through the thermodynamic analysis, it is possible to obtain a useful orientation regarding the reaction conditions, and also for the evaluation of the catalyst performance.

2.3.
Methanation Catalysts (CO_2 and CO)

Methanation catalysts commonly consist of active metal particles dispersed on metal oxide supports. Active metals such as Ni, Fe, Co, Ru, Rh, Pt, Pd, W, Mo and various oxide supports (Al_2O_3, SiO_2, TiO_2, SiC, ZrO_2, CeO_2) have been investigated in the methanation of CO_2 and CO for SNG production [17].

2.4.
Active Components

Many metals have been studied in the CO_2 methanation. It has been found that they obey the following decreasing activity order Ru> Ni> Fe> Co> Rh> Pd> Ir, [18]. Ru is undoubtedly the most active for the methanation reaction with the disadvantage of being very expensive. Ni is an alternative, being cheaper and still very active. The activity and selectivity of the supported Ni catalyst is influenced

by the content of the metal present, by the dispersion of the metal on the support, and by the interaction between metal and support [17,19].

Although Ni catalysts are preferred in the methanation reaction, there are still some practical problems, such as: carbon deposition, sintering, and sulfur poisoning during the production of SNG [17].

Inui et al. [20] investigated the deactivation by deposition of coke (carbon) and reported that it can be prevented by two options:

1. Optimizing the operating conditions by adjusting the reaction temperature or pressure by increasing the H_2 / CO_2 ratio, or by adding steam to the reagents [12,17].

2. Modifying the catalyst by creating a metal alloy (in the case of nickel it may be Ni-Fe) and adding promoters such as MgO, Sn and CeO_2 [17, 21-22].

On the other hand, pure iron has little activity and selectivity for the methanation reaction. However, when combined with Ni, in the form of Ni-Fe alloy, it presents high activity for methanation, surpassing the monometallic catalyst [23].

Rahmani et al. [24] studied Ni catalysts supported in γ-Al_2O_3 with different Ni loads, in the methanation of CO_2. The results obtained when the Ni content was increased from 10 to 25% wt showed a decrease in the specific surface area of the catalysts, and an increase in nickel crystallite size from 12 to 24 nm. In addition, an increase in the nickel content increased the reducibility and enhanced the activity toward methane. The methanation reaction involved the adsorption and dissociation of H_2, CO, CO_2.

2.5.
Support

Besides the promotion of the metal dispersion by increasing the contact area between reagents and active sites, the support plays an important role interacting with CO_2, CO, and H_2, especially when oxygen vacancies are present [25]. Al_2O_3, SiO_2, ZrO_2, TiO_2, and CeO_2 are among the most common used

supports. Every support is different, and influences in a particular manner the activity, selectivity, and stability of the catalyst [17].

Aziz et al. [26] studied the influence and interaction of MSN (Mesoporous SiO_2 nanoparticles) support in the methanation reaction. They showed that CO_2 and H_2 are adsorbed and dissociated on metal sites to form CO, O and H atoms, followed by migration onto the MSN surface. CO then interacted with MSN surface to form bridged carbonyl and linear carbonyl, while the presence of H atom facilitated the formation of bidentate formate. These three species could be associated with the formation of methane. These results suggest that the support is participating in the reaction.

Al_2O_3 γ-phase has been widely investigated due to its surface area, developed pore structure and well-characterized surface acid–base properties. Garbarino et al. [27] studied the catalytic behavior of Ni unsupported nanoparticles and Ni supported on γ-Al_2O_3 in the CO_2 methanation. It was found that Ni unsupported nanoparticles had a high selectivity for CO and poor selectivity for CH_4. On the contrary, Ni supported on γ-Al_2O_3 exhibited higher selectivity for methane, suggesting that the support surface and the support/metal interfaces may play an important role during the reaction. The influence of the size of the Ni particles in the methanation reaction was also investigated in this work suggesting that the catalyst containing small Ni particles obtained by reducing moderate loading precursor are very selective to methane without CO formation, whereas the larger Ni particles, due to higher Ni loadings, generate the higher selectivity toward CO.

Gao et al. [5] investigated the correlation between phase structures and surface acidity of γ-Al_2O_3 supports calcined at different temperatures (600-1200 °C), and the catalytic performance of Ni/Al_2O_3 catalysts in the production of SNG via CO methanation. They observed that γ-Al_2O_3 calcined at 1200 °C exhibited better activity and stability in comparison with γ-Al_2O_3 calcined at lower temperatures, this enhancement was due to an increase in the Ni oxide particle size with the weakening of the metal-support interaction, making the catalyst

25

more reducible. It is worth stressing that this result related to the CO methanation is opposite to the one described above for the CO_2 methanation.

TiO_2 is highly active for the methanation reaction. Ni is able to enter in the TiO_2 lattice, which creates oxide vacancies and facilitates hydrogen adsorption and spillover (spillover phenomenon is the transport of a species adsorbed or formed on a surface onto another surface) from nickel to support. This phenomenon improves the catalytic performance [17].

ZrO_2 support is similar to TiO_2 improving the dispersion of Ni as well as the hydrogen-promoted dissociation of carbon monoxide [28]. Da Silva et al. [29] studied the methanation of CO over Ni/ZrO_2 catalyst. The authors observed that this oxide not only is able to adsorb CO, but also to promote the hydrogen and CO spillover phenomenon. They identify the presence of very active sites of CO methanation on the ZrO_2 surface.

In a similar way, Centi et al. [30] studied the methanation of CO_2 employing Ni–Fe/(Mg, Al)O_x bimetallic catalysts derived via mixed hydrotalcite precursors, where iron exhibits a significant influence on both activity and selectivity. Iron promoted the generation of small particle sizes, facilitated CO dissociation, and increased the basicity of the catalyst. Centi and collaborators also studied the influence of the iron content on particle size, CO dissociation energy, and support basicity. They identified the most appropriate metal content to be added to the Ni/(Mg, Al)O_x in order to improve activity, selectivity, and stability, is a small amount of Fe (Fe/Ni = 0.1). It was found that when Fe content exceeded this proportion the activity and selectivity to methane of the catalyst decreases. The reduction temperature during the pretreatment plays an important role since there exist strong interactions among Ni and hydrotalcite derived molecules in the catalyst matrix requiring higher reduction temperatures 600-900°C, as shown in Figure 6.
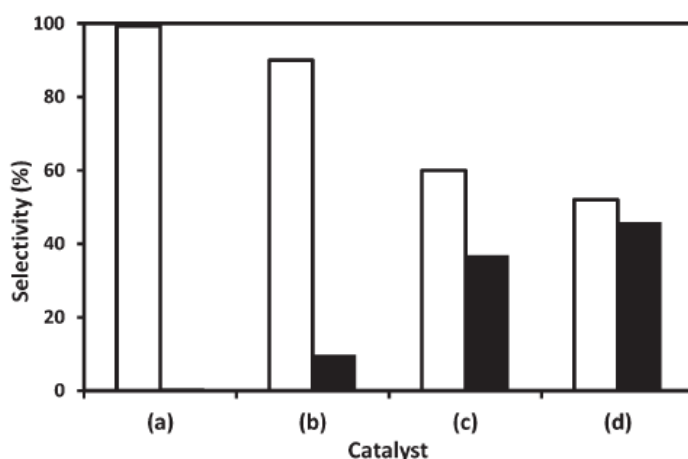
Figure 6. Selectivity of CH4 (□) and CO (■) at different reduction temperatures: a) Ni–Fe/(Mg, Al)Ox (Fe/Ni = 0.1) at 600 °C, b) Ni–Fe/(Mg, Al)O$_x$ (Fe/Ni = 0.1) at 500 °C, c) Ni–Fe/(Mg, Al)Ox (Fe/Ni = 0.5) at 600 °C, d) Ni–Fe/(Mg, Al)Ox (Fe/Ni = 0.5) at 500 °C. (Adapted from Centi et al. [30]).

Baldauf-Sommerbauer et al. [31] studied the methanation of CO_2 over a Ni/MgO catalyst generating interesting results. The CO_2 methanation on the Ni/MgO catalyst used in their work is proposed to proceed in a sequential reaction scheme of reverse water-gas-shift followed by CO methanation. Finally, constant conversion of 70% at a feed flow rate of 1000 cm^3_{STP} min^{-1} (feed composition H_2:CO_2:N_2 =4:1:5), and a selectivity of >99% at 330 °C was demonstrated over a total period of 210 h.

CeO_2 has the ability to change its oxidation state from Ce^{4+} and Ce^{3+}. When this reduction takes place, oxygen vacancies emerge. The superficial vacancies created in CeO_2 after reduction at high temperature could enhance the carbon dioxide methanation activity due to its interaction with CO_2 molecule. Wang et al. [25] employed operando XANES, IR, and Raman methodology to study the CO_2 methanation reaction catalyzed by Ru/CeO_2 (with oxygen vacancy in CeO_2) and Ru/α-Al_2O_3 (without oxygen vacancy) the study reveals that CO_2 methanation over Ru/CeO_2 undergoes by the formate route on the surface of CeO_2 in which Ce^{3+}, surface hydroxyl, and oxygen vacancy jointly participate in this route. The formate dissociation catalyzed by oxygen vacancy is the rate-determining step. In contrast, CO_2 methanation undergoes CO route over (RWGS)

Ru surface in $Ru/\alpha-Al_2O_3$ with the absence of oxygen vacancy, suggesting that the CO_2 methanation mechanism is dependent on the catalytic system.

Table 2 presents the performance of some Ni based catalyst employed in the methanation of CO_2, due to the high amount of operational variables, it is not trivial to measure the performance of each catalyst but it can be a comparison based on similar GHSV (gas hourly space velocity) at similar temperatures. The catalyst from Takano et al. [32], 50% $Ni/(ZrO_2 +Ca)$, has the highest activity of all with a GHSV of 400,000 mL $g^{-1}h^{-1}$ and a CO_2 conversion of 85%. Moreover, since the catalytic tests from authors Aziz et al. [26], Garbarino et al. [27], and X. Jia et al. [33] have similar GHSV (50,000-60,000 mL$g^{-1}h^{-1}$) among them it can be noted that the catalyst 16%Ni/y-Al_2O_3 (%XCO_2 = 50) exhibited the lower activity of all, since the catalytic tests were done at higher temperature (400°C) obtaining less CO_2 conversion when compared with 8.68%Ni/ZrO_2 (%XCO_2 = 92) and 5%Ni/MSN (%XCO_2 = 64). It is difficult to compare these last two catalysts since they exhibited different operation temperatures.

A third comparison can be done over the catalyst whose GHSV range from (4,900-6,000 mL $g^{-1}h^{-1}$), Da Silva et al. [29] whose 10%Ni/ZrO_2 catalyst leads this range with a CO_2 conversion of 92%, followed by the 5%Ni/ZrO_2-Al_2O_3 from J. Lin et al. [34] with a CO_2 conversion of 70% and finally the 11% Ni/MgO catalyst from Baldauf-Sommerbauer et al. [31] with a slight lower CO_2 conversion of 65%. It can be observed that all of these catalysts present very high selectivity to methane.

Table 2. Comparison among different Ni based catalyst employed in the CO_2 methanation reaction.

Authors Reference	Catalyst	Catalyst Preparation	Temp °C	GHSV mL $g^{-1}h^{-1}$	H_2/CO_2	Selectivity (%)		%XCO$_2$	BET m$_2$/g
						CH$_4$	CO		
AZIZ et al. [26]	5%Ni/MSN	Wet impregnation	300	50,000	4/1	99.9	0.1	64	879
	5%Ni/y-Al$_2$O$_3$	Wet impregnation	300	50,000	4/1	95.2	4.8	28	210
	5%Ni/SiO$_2$	Wet Impregnation	301	50,000	4/1	96.6	3.4	42	158
Rahmani et al. [24]	10%Ni/ y-Al$_2$O$_3$	Wet Impregnation	350	9,000	3.5	93	7	68	177
Garbarino et al. [27]	16%Ni/ y-Al$_2$O$_3$	Wet Impregnation	400	52,300	5/1	100	0	50	137
Da Silva et al. [29]	10%Ni/ZrO$_2$	Wet Impregnation	327	5,600	4/1			92	76
	10%Ni/SiO$_2$	Wet Impregnation	327	5,600	4/1			68	73
Ashok et al. [35]	10% Ni/CeO$_2$-ZrO$_2$	AE method (NO$_3$ and NH$_3$)	350	20,000	4/1	95	5	54	78
Takano et al. [32]	50% Ni/(ZrO$_2$+Ca)	Wet impregnation	350	400,000	4/1			85	32
J. Lin et al. [34]	5%Ni/ZrO$_2$-Al$_2$O$_3$	Sol gel method	350	6,000	4/1	99	1	70	198
X. Jia et al. [33]	8.68% Ni/ZrO$_2$	Wet Impregnation	350	60,000	4/1	100	0	92	70
Baldauf-Sommerbauer et al. [31]	11% Ni/MgO	Wet Impregnation	325	4,963	4/1	100	0	65	67

29

2.6.
Recent studies on Reverse Water Gas Shift Reaction (RWGS)

Rodrigues et al. [36] studied the RWGS employing Ni/ Mg(Al)O and SiO_2. They verified that the Ni/ Mg(Al)O systems are much more active than the latter and the Mg(Al)O support improved the activity of the catalyst. The CO formation rate on Ni/SiO_2 is lower than on Ni/ Mg(Al)O systems, and the CH_4 formation rate on Ni/ Mg(Al)O catalysts is higher than on Ni/SiO_2. The authors also suggested that Mg(Al,Ni)O vacancies and Ni^0 are active species participating in the reduction of CO_2 to CO during the RWGS.

Sun et al. [37] studied a series of Ni-based catalysts supported on $Ce_{1-x}Zr_xO_2$. The $Ni/Ce_{1-x}Zr_xO_2$ catalyst provides high activity, stability and selectivity in the conversion of CO_2 to CO at high temperature. $Ce_{1-x}Zr_xO_2$ solid solution is formed by co-precipitation and Ni is able to migrate into the $Ce_{1-x}Zr_xO_2$ lattice. The authors consider Ni species on catalyst surface as the active sites for RWGS, The investigation reveals that CO_2 conversion reaches 50% and maintains stable after 80 h of reaction over 3% Ni/ $Ce_{1-x}Zr_xO_2$. The selectivity to CO reaches 95%. When the Ni content is increased to 10%, the CO selectivity observed is almost 100% at 750 °C.

Zonetti et al. [38] prepared catalysts based on $Ni_xCe_{0.75}Zr_{0.25-x}O_2$ and tested their performance in the RWGS. It was shown that Ni is able to be incorporated into the $Ce_{0.75}Zr_{0.25}O_2$ lattice by co-precipitation or by impregnation, generating very active RWGS catalysts. The NiCeZr mixed oxide which was prepared by co-precipitation is also a very promising component of catalytic systems employed in reactions where the RWGS is one of the steps, as for instance, processes which generate hydrocarbons from CO_2. The authors inferred that the higher the reducibility of the mixed oxides based on Ce, Zr and Ni, the higher the activity in the RWGS. The authors suggested that the high activity of the NiCeZr catalyst is related to its higher concentration of vacancies which are created due to the insertion of Ni into the CeZr lattice.

Luhui et al. [39] studied the performance of a Ni/CeO_2 catalyst in the RWGS. Their catalysts were prepared employing two different procedures. The first used a mixture of Na_2CO_3, NaOH (Na_2CO_3:NaOH; 1:1 ratio) and cerium nitrate which generates oxygen vacancies leading to the formation of cerium carbonate hydroxide as precursor. The other used the same precursors independently (without mixing Na_2CO_3 and NaOH) which led to less or no formation of oxygen vacancies. It was found that the catalyst with oxygen vacancies exhibited the best catalytic performance for the RWGS. The authors employed the H_2-TPR to characterize the oxygen species, and concluded that there exist two peaks at a temperature lower than 300°C that are related to the generation of oxygen vacancies.

B. Lu et al. [40] investigated the performance of mesoporous NiO/CeO_2 as a catalyst for the RWGS and concluded that the CO_2 conversion increased when the temperature and NiO amount were also increased. With less than 3 wt% NiO, the NiO particles were monodispersed in mesoporous CeO_2. This system exhibits 100% of CO selectivity, regardless of temperature. NiO particles aggregated in the presence of more than 3.5 wt% NiO, in this case the CO selectivity is 100% at 700 °C, while at temperatures below 650 °C the CO selectivity was around 96%.

2.7.
Role of the oxygen vacancies

Ashok et al. [35] have studied the CO_2 methanation over Ni supported on $Ce_xZr_{1-x}O_2$. They suggested the incorporation of Ni into the CeO_2 lattice, which resulted in the generation of oxygen vacancies. They proposed that the adsorption of oxygenate species is enhanced by the oxygen vacancies. The authors employed a CO-TPR to determine the presence of oxygen vacancies by monitoring the formation of CO_2 during this analysis by considering the reaction of the CO molecule with an oxygen from the surface lattice of the CeO_2.

Takano et al. [32] employing Ni/ZrO_2 showed that the isomorphic substitution of Zr^{4+} by the Sm^{3+}, Y^{3+}, Ni^{2+} an Ca^{2+} cations in the ZrO_2 lattice improves the performance of the catalyst due to the generation of oxygen

vacancies. They associated the oxygen vacancies with the improvement of CO_2 adsorption and enhancement of the catalytic activity. The authors employed TPD-CO_2 and H_2-TPR to identify the oxygen vacancies by disclosing the presence of strong CO_2 adsorption sites which are related to the presence of oxygen vacancies.

Wang et al. [25] using Ru/CeO_2 and steady-state isotope transient kinetic analysis observed that the CeO_2 vacancies are active sites of the rate-determinant step of the CO_2 methanation, i.e., the formate dissociation to methoxide species. The authors employed operando Raman to monitor the concentration of oxygen vacancies in the reduction process and the following reaction process. They monitor the intensity ratio between two bands at ($\sim$570 cm^{-1}) and ($\sim$460 cm^{-1}) which is related to the concentration of oxygen vacancy in CeO_2.

X. Jia. et al. [33] employing plasma in the Ni/ZrO_2 catalyst preparation suggested that anionic vacancies are associated with the CO_2 activation, which leads to an enhancement in the activity of the catalyst. The author employed XPS analysis to characterize oxygen vacancies by reasoning in the following manner: the Zr $3d_{3/2}$ and Zr $3d_{5/2}$ peaks centered at 184.41 eV and 182.02 eV are assigned to Zr^{4+}. Two other peaks with slightly lower binding energies, i.e. 183.21 eV and 181.30 eV suggest the partial reduction of Zr^{4+} towards Zr^{x+} (x<4). The authors also analyzed the O1s core level which exhibited two peaks. The one at 529.88 eV originates from the lattice oxygen of ZrO_2, and the minor peak at the higher binding energy of 531.88 eV normally belongs to oxygen anions on the oxygen-deficient $ZrO_{x/2}$ surface (oxygen defect).

Recently, J. Lin et al. [34], employing mesoporous Ni/Al_2O_3-ZrO_2 catalysts prepared by sol-gel method suggested that both Ni and oxygen vacancies play a crucial role in the improvement of the catalytic activity and CH_4 selectivity. These authors suggested that CO_2 and CO dissociations occur on oxygen vacancies. They employed XPS analyses to verify the presence of oxygen vacancies

According to the literature, oxygen vacancies are very relevant for the CO_2 methanation. Although there are many interesting propositions about its main role in this reaction, there is no consensus about this topic.

2.8.
Mechanisms Proposals

Although the methanation of CO_2 seems to be a simple reaction, discussions about the intermediates fall into two main categories: this reaction occurs via hydrogenation of formates and carbonates, or the first step is the RWGS followed by the CO methanation generated by the first step. There is a lot of discrepancy between the authors, some studies related to this subject are shown below.

Aldana et al., [2] studied the mechanism for CO_2 methanation over Ni-ceria-zirconia catalysts. They suggest that this reaction does not require CO as reaction intermediate. Therefore, H_2 would be dissociated on Ni^0 sites while CO_2 would be interacting on the ceria-zirconia support to form carbonates which would be hydrogenated into formates and further into methoxy species, which decompose generating CH_4. This mechanism involves basic sites of the support for the adsorption of CO_2 and implies a stable metal-support interface, Figure 7 shows the mechanism proposed by Aldana and collaborators The high activity of the catalyst is related to the interaction between CO_2 and the support. This contrasts with the low activity of a Ni-silica catalyst where the CO_2 and H_2 interacts only with the Ni metallic particles.
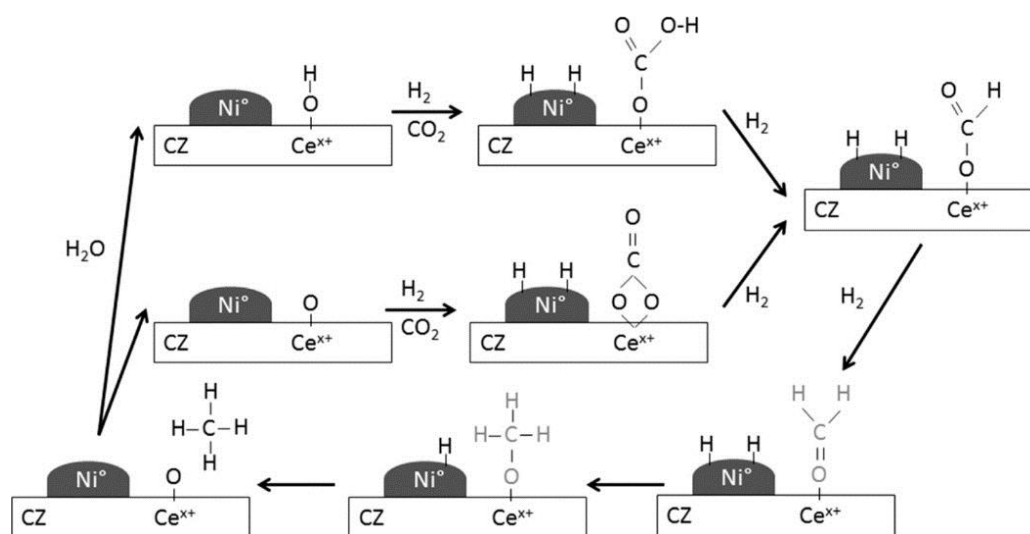
Figure 7. Reaction mechanism proposed on $Ni/Ce_{1-x}Zr_xO_2$ sample. Adapted from Aldana et al. [2].

Pan et al., [41] agree with Aldana et al. [2] They evaluated two catalysts $N/\gamma-Al_2O_3$ and $Ni/Ce_{0.5}Zr_{0.5}O_2$, both catalysts differ in their basic sites, $Ni/\gamma-Al_2O_3$ catalyst has both weak and strong basic sites while $Ni/Ce_{0.5}Zr_{0.5}O_2$ shows weak and medium basic sites according to $TPD-CO_2$. It was noted that CO_2 adsorbed on strong basic sites can't desorb from the $Ni/\gamma-Al_2O_3$ surface until 700 °C staying as spectators during the reaction, when the temperature ranged from 220°C-400°C, therefore, the activity of the $Ni/\gamma-Al_2O_3$ is lower than that of the $Ni/Ce_{0.5}Zr_{0.5}O_2$ catalyst. Pan and collaborators proposed the following mechanism (Figure 8) for the CO_2 methanation on $Ni/Ce_{0.5}Zr_{0.5}O_2$: CO_2 is adsorbed on hydroxyl generating hydrogen carbonates, which are hydrogenated to form bidentate formate species, whereas CO_2 adsorption on surface oxygen results in the monodentate carbonates which are hydrogenated to monodentate formate species. Since monodentate formate is hydrogenated faster to methane than bidentate formate, hydrogenation of monodentate formate is assumed to be the main reaction route on $Ni/Ce_{0.5}Zr_{0.5}O_2$. For CO_2 methanation on $Ni/\gamma-Al_2O_3$, hydrogen carbonates and bidentate formate are the main intermediate species, respectively, indicating hydrogenation of bidentate formate as main reaction route.

34
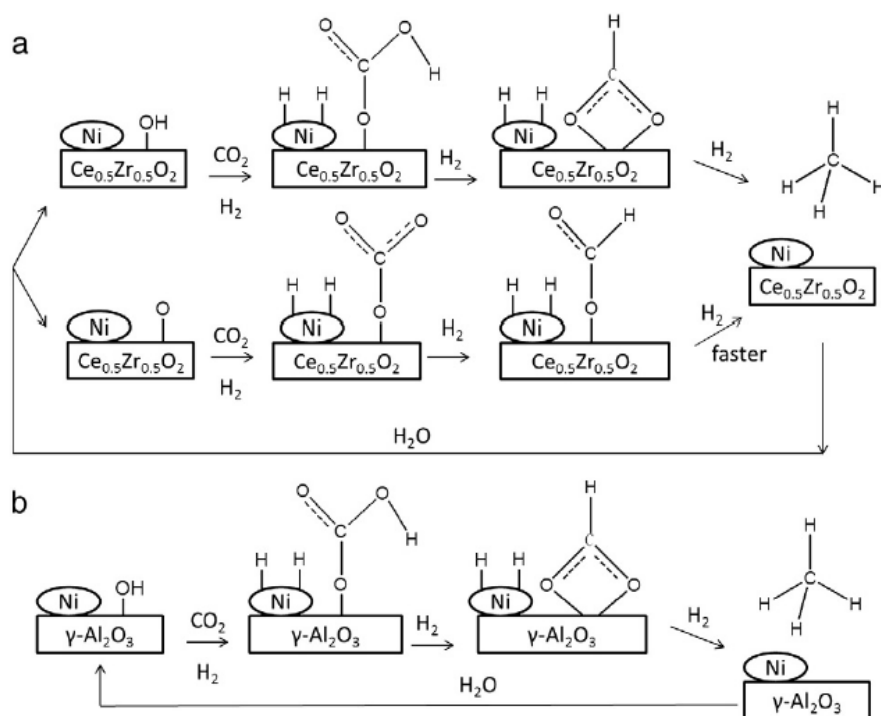
Figure 8. Reaction mechanism proposed on: a) $Ni/Ce_{0.5}Zr_{0.5}O_2$, b) $Ni/\gamma-Al_2O_3$ (adapted from Pan et al. [41]).

On the other hand, Eckle et al, [42] studied the methanation reaction over Ru/zeolite and Ru/Al_2O_3 using in situ diffuse reflectance infrared Fourier transform spectroscopy (DRIFTS) measurements. They monitored the CO_{ad} band intensity, $CH_{4,ad}$, HCO_{ad} formate band intensity, and the CH_4 formation rate under steady-state conditions. They suggest that the path proceeds via formation and further methanation of CO_{ad}. The authors proposed that the mechanism, cannot be via formate because the decomposition rate of these species is very slow compared to the adsorption of CO_2 to form CO_{ad} and O_{ad}, which subsequently reacts to CH_4 and H_2O.

Akamaru et al., [43] studied the CO_2 methanation reaction on a Ru nanoparticle supported on a TiO_2 catalyst using the density functional theory (DFT). They proposed a mechanism in which initially, the adsorbed CO species are formed via dissociation of adsorbed CO_2 and/or COOH species. The COOH species are generated by hydrogenation of adsorbed CO_2. The adsorbed CO

species is then hydrogenated to CHO and/or CHOH species, and the OH group is released. Finally, CH_4 is generated via further hydrogenation. Figure 9 shows the mechanism proposed along with the potential energy barrier of each species considering that the reaction occurs at the top surface of the catalyst. The authors described two limiting steps for the CO_2 methanation reaction on the Ru surface. (1) The formation of CHO species from adsorbed CO, which has the largest reaction energy of 24.5 kcal/mol, and a potential energy barrier of 28.9 kcal/mol, as shown in Figure 9. (2) The hydrogenation reaction of CH_3 to CH_4, which has the highest potential barrier of 29.0 kcal/mol for the methanation reaction on the Ru surface (also shown in Figure 9).
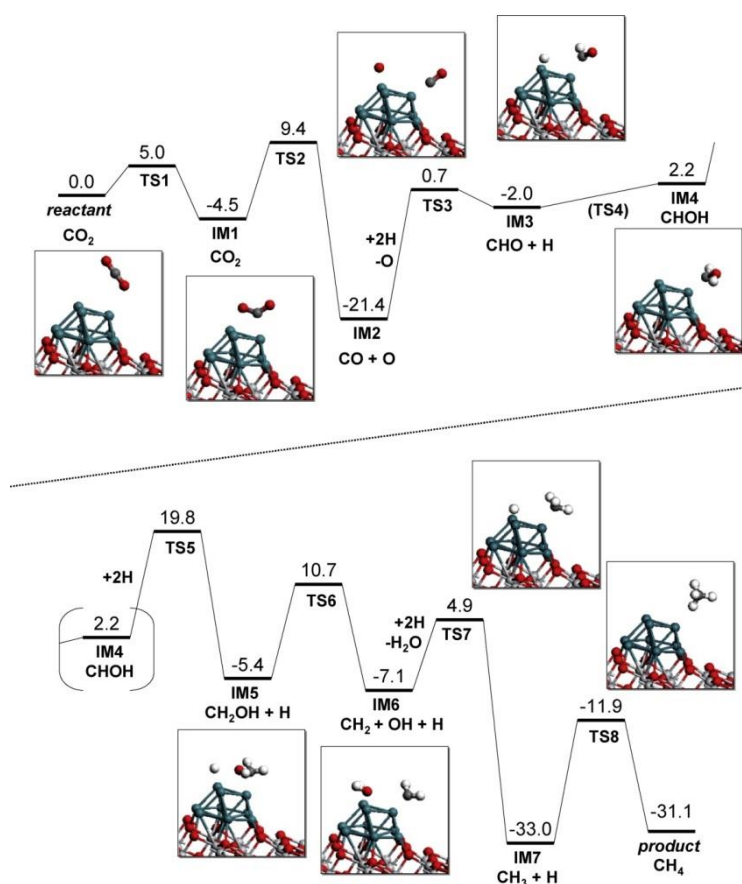
Figure 9. Potential energy diagram for CO_2 methanation on the top of the Ru nanoparticle/TiO_2 catalyst considering CO as intermediate. Each reactant, product and intermediate structures are also shown (adapted from Akamaru et al. [43]).

Karelovic & Ruiz [44] investigated the CO_2 methanation at low temperature ($T \leq 200$ °C) over a catalyst prepared by a physical mixture of Rh(2 wt %)/γ-Al_2O_3 and Pd(5 wt %)/γ-Al_2O_3 catalysts The nature and reactivity of reaction intermediates was studied by in situ DRIFTS performed at steady state and transient mode. Rh carbonyl hydride was the most abundant carbon-containing species adsorbed on Rh, whereas bridge-bonded CO dominated Pd sites. The proposed mechanism of reaction over Rh proceeds by the surface reaction of H(ads) and CO(ads) species (the latter coming from CO_2 dissociation on the metal surface) to form a hydrogenated CO intermediate that is subsequently hydrogenated to methane as shown in Table 3a . Karelovic & Ruiz [45] also studied the methanation of CO_2 employing a Rh/TiO_2 catalyst. The authors employed kinetic data with operando DRIFTS to evaluate to reaction path. They suggested that direct CO dissociation (shown in Table 3b) is not likely to be the dominant mechanism of reaction. Again the authors considered that the reaction path proceeds via H-assisted CO dissociation as shown in Table 3a. This consideration took place by predicting the reaction order. The formation of CH from H_2CO is considered the rate determining step in this reaction.

Table 3. Presents two proposed mechanism for CO_2 methanation. (a) H assisted carbon monoxide dissociation. (b) Un-assisted carbon monoxide dissociation. Adapted from Karelovic & Ruiz [45] .

(a) H-assisted carbon monoxide dissociation	(b) Unassisted carbon monoxide dissociation
1. $CO_2 + 2* \leftrightarrow CO* + O*$	1. $CO_2 + 2* \leftrightarrow CO* + O*$
2. $H_2 + 2* \leftrightarrow 2H*$	2. $H_2 + 2* \leftrightarrow 2H*$
3. $CO* + 2H* \leftrightarrow H_2CO* + 2*$	3. $CO* + * \rightarrow C* + O*$ (RDS)
4. $H_2CO* + * \rightarrow CH* + OH*$ (RDS)	4. $C* + H* \leftrightarrow CH* + *$
5. $CH* + 3H* \leftrightarrow CH_4 + 4*$	5. $CH* + 3H* \leftrightarrow CH_4 + 4*$
6. $O* + H* \leftrightarrow OH* + *$	6. $O* + H* \leftrightarrow OH* + *$
7. $OH* + H* \rightarrow H_2O + 2*$	7. $OH* + H* \rightarrow H_2O + 2*$

Ren et al. [46] studied the different mechanisms of CO_2 methanation on Ni (111) surfaces also using density functional theory. They proposed the following

optimal path shown in Figure 10: CO_2 firstly decomposes into CO and O on the Ni(111) surface. Then CO decomposes into C and O and C hydrogenates to CH_4, therefore, the elementary reaction $CO \rightarrow C + O$ is the rate-determining step (RDS) in this path.

$$H_2 + 2* \rightarrow 2H*$$

$$CO_2 + * \rightarrow CO_2*$$

$$CO_2* + * \rightarrow CO* + O*$$

$$CO* + * \rightarrow C* + O*$$

$$C* \xrightarrow{+H*} CH* \xrightarrow{+H*} CH_2* \xrightarrow{+H*} CH_3* \xrightarrow{+H*} CH_4 + *$$

$$O* \xrightarrow{+H*} OH* \xrightarrow{+H*} H_2O* \rightarrow H_2O + *$$
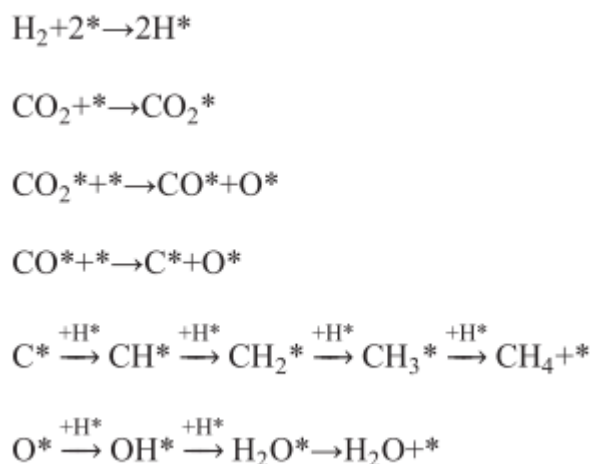
Figure 10. Proposed mechanism for the CO_2 methanation Ni(111) surface
(adapted form Ren et al.[46])

Aziz and collaborators [47] studied the reaction mechanism of the CO_2 methanation using a series of metal catalysts (Rh, Ru, Ni, Fe, Ir, Cu, Zn, V, Cr, Mn, Al and Zr) supported on MSN by employing in situ FTIR spectroscopy analyses. They suggested the mechanism as follows: firstly, CO_2 and H_2 were adsorbed onto metal sites, followed by dissociation to form CO, O and H atoms, and migration onto the MSN surface. The CO then interacted with oxide surfaces of the MSN to form bridged carbonyl and linear carbonyl. Bidentate formate was also formed through the interaction with atomic hydrogen. Meanwhile, the O atom spilt over onto the surface of the MSN and was stabilized in the oxygen vacancy site near the metal site. The adsorbed oxygen then reacted with atomic hydrogen to form hydroxyl on the MSN surface in which a further reaction with another atomic hydrogen formed a water molecule. Finally, the adsorbed carbon species were further hydrogenated to methane and another water molecule. The authors suggests that bidentate formate species could be the main intermediate for CO_2. Figure 11 shows a scheme for the proposed mechanism.
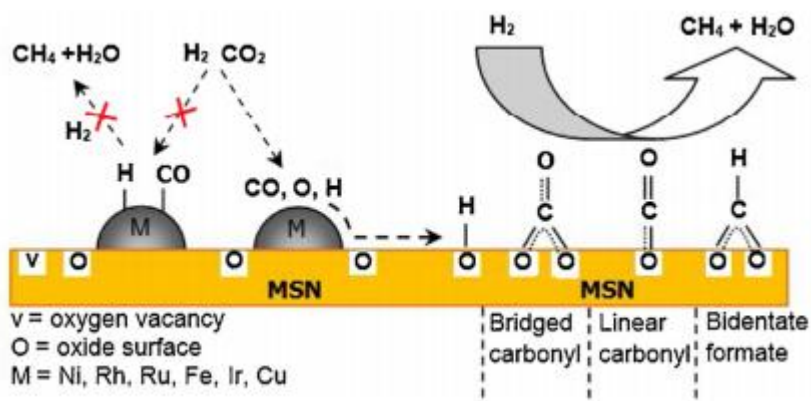
Figure 11. Proposed mechanism of CO_2 methanation on M/MSN (extracted from Aziz et al. [47]).

2.9.
Literature review final remarks

The methanation of CO_2 is a complex reaction as discussed earlier in the literature review section. The behavior of the support is not clear during the methanation reaction. Does the CO_2 methanation occurs via formates and carbonates, or does it transform into CO which is subsequently hydrogenated to CH_4. According to the literature, the oxygen vacancies are very relevant for the CO_2 methanation. Although there are many interesting propositions about its main role in this reaction, there is no consensus about this topic.

Previous work of our group showed that adding Zn to the monoclinic ZrO_2 oxide improved significantly the redox properties of the catalyst employed in the RWGS due to the generation of oxygen vacancies [48]. It was also observed that Ni supported on monoclinic ZrO_2 is a very active catalyst for the CO and CO_2 methanation [29]. It was proposed that O vacancies of the support play an essential role in the methanation reactions when Ni/ZrO_2 is employed.

3.
Objectives

The main goal of this work is to contribute to the description of the role of the catalyst support in the CO_2 methanation.

Specific aims:

1) Describe the role of the oxygen vacancies in the methanation of CO_2.
2) Contribute to the understanding of the CO_2 methanation mechanism.
3) Contribute to the description of the promoter (Ca) role of the Ni/zrO_2 catalysts behavior.

4.
Methodology

4.1.

Preparation of catalysts

The Ni/ZrO_2, $Ni/CaZrO_2$ Ni/SiO_2, Ni/MgO and $Ni/Mg(Al)O$ catalysts were synthesized by the wet impregnation method using $Ni(NO_3)_2 \cdot 6H_2O$ (Aldrich). The Ni concentration for Ni/ZrO_2 and Ni/SiO_2 catalysts was 10, 5, 2 and 0.5 wt.%, for $Ni/Mg(Al)O$ was 10 and 5 wt.%. The oxides ZrO_2 (monoclinic) and SiO_2 (amorphous) were supplied by Norpro Saint Gobain, the support $Mg(Al)O$ by SASOL ($MgO:Al_2O_3 = 70:30\%$).

In the wet impregnation method, a suspension was prepared containing the precursor salt and the support. This suspension was placed in a round bottom flask coupled to a rotary evaporator. The whole system was subjected to vacuum. The flask containing the suspension was kept spinning and immersed in a thermal bath at 80 ^{o}C. The material resulting from this drying was placed in an oven at 100 ^{o}C for 18 h. The material was then calcined at a heating rate of 5 ^{o}C min^{-1} to 500 ^{o}C and held at this temperature for 5 h with an air flow of 20 mL min^{-1} [29].

In the case of $Ni/CaZrO_2$, ZrO_2 was doped with 0.7wt% Ca, employing $Ca(NO_3)_2$, before Ni impregnation. Initially, a suspension was prepared containing $Ca(NO_3)_2$ and the monoclinic ZrO_2 support. This suspension was placed in a round bottom flask coupled to a rotary evaporator. The whole system was subjected to vacuum. The flask containing the suspension was kept spinning and immersed in a thermal bath at 80 ^{o}C. The material resulting from this drying was placed in an oven at 100 ^{o}C for 18h. The material was then calcined at a heating rate of 5 ^{o}C min^{-1} to 500 ^{o}C and held at this temperature for 14h in air flow (20 mLmin^{-1}). Afterwards, 5wt% of Ni was impregnated to the $CaZrO_2$ support, dried and finally calcined at a heating rate of 5 ^{o}C min^{-1} to 500 ^{o}C and held at this

temperature for 5 h in air flow (20 mLmin^{-1}). The grain size was standardized by employing a strainer with an opening of 0.053 mm (ABNT 270).

4.2.
Passivation procedure of the catalysts

X-Ray analyses were carried out employing reduced-passivated catalysts as well as *in situ* reduced catalyst. The samples Ni/ZrO$_2$, Ni/SiO$_2$ and Ni/Mg(Al)O were submitted to a passivation procedure. Firstly, the samples Ni/ZrO$_2$ and Ni/SiO$_2$ were heated at 500 °C for 30 min under N$_2$ flow (30 mLmin^{-1}). Afterwards, the samples were reduced at 500°C for 30 min under pure H$_2$ flow (30 mLmin^{-1}). The Ni/Mg(Al)O was heated at 700 °C for 30 min under N$_2$ flow (30 mLmin^{-1}) and reduced at 700 °C for 60 min under pure H$_2$ flow (30 mLmin^{-1}). Then, the catalysts were cooled down to room temperature under N$_2$ flow. The passivation procedure was carried out around -60°C using a cryogenic cooling bath under 4% O$_2$/N$_2$ flow (30 mLmin^{-1}) for 1 h. Finally, the solids remained at room temperature for 1 h under 4% O$_2$/N$_2$ flow [36].

4.3.
Characterization of the prepared catalysts

4.3.1.
Chemical Composition by X-ray fluorescence

The chemical composition analyses were carried out using a S8 Tiger Bruker wavelength dispersive X-ray fluorescence spectrometer (WC-XRF) equipped with a rhodium tube operated at 30-60 kW. The analysis was done with powder sample using a semi-quantitative method (QUANT-EXPRESS/Bruker) in order to determine the metal content incorporated to the prepared catalysts and compare it with the nominal metal content.

4.3.2.
Textural Properties

The specific surface area of the catalysts and supports were evaluated from Brunauer−Emmett−Teller (BET) method, using a Micrometrics ASAP 2010

equipment. The samples were treated at 100 °C for 24 h. Thereafter, they were submitted to an *in situ* under vacuum treatment at 150 °C for 2 h. The N_2 adsorption was carried out at -196 °C.

4.3.3.
Cyclohexane dehydrogenation reaction

The dehydrogenation reaction of cyclohexane is a model reaction insensitive to structure and it is used to generate data proportional to the metallic area. The rate of cyclohexane dehydrogenation is used in this work as an indirect measure of the Ni surface area [49]. The Ni/ZrO_2 and Ni/SiO_2 samples were heated at 500 °C (5 °C/min) for 30 min under N_2 flow rate of 30 mL min^{-1}. Then, using this same temperature they were reduced with pure H_2 for another 30 min. The Ni/Mg(Al)O catalyst was heated at 700 °C for 30 min under N_2 flow, and it was reduced with pure H_2 at 700°C for 1 hour [36]. This reaction was carried out at atmospheric pressure using a conventional system with a fixed-bed micro-reactor. It was monitored by on-line gas chromatography equipped with a flame ionization detector (FID). The cyclohexane vapors were generated in a saturator (285 K) using H_2 as a carrier gas (90 mL min^{-1}) [29]. The H_2/C_6H_{12} ratio was 13. It is important to mention that similar values of the rate of cyclohexane dehydrogenation suggest similar metallic area among the catalyst being compared.

4.3.4.
Temperature Programmed Reduction (TPR)

Temperature programmed reduction tests (TPR) are used to evaluate the reducibility of the catalyst [27]. The peaks of the TPR profile also reveals empirical information related to species that are being formed during the reduction process. The temperature programmed reduction (TPR) analyses were carried out employing an AutoChem II Micromeritcs equipment which is equipped with a TCD detector. The Ni/ZrO_2 $Ni/CaZrO_2$ and Ni/SiO_2 catalysts were heated at 500 °C under N_2 flow (30 mLmin^{-1}) for 30 min. After that, they were reduced at 500 °C during 30 min with 10 %H_2/N_2 flow, purged for 15 min under N_2 flow and then calcined at 500 °C for 30 min under 30 mLmin^{-1} of synthetic air flow rate. The same procedure was applied to Ni/Mg(Al)O

modifying only the temperature to 700 °C and prolonging the reduction time to 1 hour. The analyses were conducted using 50 mLmin^{-1} of 10 % H$_2$/N$_2$ mixture, from 30 to 900 °C (10 °C min^{-1}).

4.3.5.
Thermal programmed desorption of CO$_2$-TPD

This analysis will help to understand the interaction between the surface of catalyst and the CO$_2$ molecule. The TPD analyzes consist of exposing the sample to a reagent at room temperature in order to provide conditions for adsorption. The CO$_2$-TPD experiments were conducted employing a micro reactor coupled to a Dycor Mass Spectrometer, Ametek Process Instruments. The Ni/ZrO$_2$, Ni/Mg(Al)O and Ni/SiO$_2$ systems (500 mg) (described in chapter 5) were heated at 500 °C (5 °Cmin^{-1}) for 30 min under a flow of He (30 mLmin^{-1}), before being reduced with 10 % H$_2$/N$_2$ under a flow rate of 30 mLmin^{-1} for 30 min. In the particular case of the Ni/Mg(Al)O, it was heated at 700 °C for 30 min and reduced at this same temperature during 60 min . All samples were cooled under 30 mLmin^{-1} He flow rate until they reached room temperature. Then, the samples were exposed to CO$_2$ (30 mLmin^{-1}) for 1 h at room temperature. After that, the TPD of CO$_2$ measurements were carried out heating the samples at 10 °Cmin^{-1} up to 500 °C, under He flow (80 mLmin^{-1}).

In the case of the Ni/ZrO$_2$ and Ni/CaZrO$_2$ systems described in chapter 6 the CO$_2$-TPD experiments were conducted employing a Micromeritics AutoChem 2920 equipment. The catalysts (100 mg) (described in chapter 6) were heated at 500 °C (5 °Cmin^{-1}) for 30 min under a flow of He (30 mLmin^{-1}), before being reduced with 10 % H$_2$/N$_2$ under a flow rate of 30 mLmin^{-1} for 30 min. Both samples were cooled under 30 mLmin^{-1} He flow rate until they reached room temperature. Then, the samples were exposed to CO$_2$ (30 mLmin^{-1}) for 1 h at room temperature. After that, the TPD of CO$_2$ measurements were carried out heating the samples at 10 °Cmin^{-1} up to 500 °C, under He flow (50 mLmin^{-1}).

4.3.6.
Electron paramagnetic resonance (EPR)

Electron paramagnetic resonance (EPR) was used to evaluate the presence of vacancies in the catalyst support. A Bruker ESP 300e spectrometer operating in the X-band (9.7GHz) was employed. The value of the microwave power, field scan and amplitude modulation were 20 mW, 0-6000G and 5G, respectively. Before the analyses, the samples (150 mg) were submitted to the following pretreatment: firstly, the ZrO_2 oxide was heated at 500 °C for 30 min under He flow (30 mLmin^{-1}); then, reduced at 500 °C for 30 min under pure H_2 flow (30 mLmin^{-1}); next, cooled down to room temperature under Ar flow (30 mLmin^{-1}). In the case of the Mg(Al)O oxide it was heated at 700 °C under He flow (30 mLmin^{-1}) for 30 min and reduced for another 60 min under pure H_2 flow (30 mLmin^{-1}); next, cooled down to room temperature under Ar flow (30 mLmin^{-1}); finally, the reactors containing the sample were carefully sealed and transported to the EPR equipment.

4.3.7.
X-ray diffraction (XRD)

X-ray diffraction patterns (XRD) of the oxide, *in situ* reduced as well as the passivated reduced catalyst were obtained using a D8-Discover diffractometer model equipped with copper tube, Kalpha radiation (lambda=0.15406 nm), nickel filter, Lynxeye solid state detector, tube tension 40 kV, and current 40 mA). The angular range varied from 10° to 90°, with increments of 0.02° and 1 s per step. A reduction chamber was coupled to the X-ray diffractometer where the samples (500 mg) were initially heated at 500 °C (5 °Cmin^{-1}) for 30 min under a flow of He (30 mLmin^{-1}). Then using this same temperature they were reduced with 2% H_2/N_2 under a flow rate of 30 mLmin^{-1} for 4 hours, afterwards the X-ray analysis was conducted. Rietveld refinement technique was employed using TOPAS software to quantitatively identify the different crystalline phases present in the samples, as well as the cell volumes and the site of occupancies.

4.3.8.
X-ray Photoelectron Spectroscopy (XPS)

XPS technique identifies the elements and their neighborhood by analyzing the energies of the photoelectrons ejected by a monochromatic X-rays. It is an extremely sensitive surface analysis technique. It provides quantitative and chemical state information from the surface of the material. X-ray photoelectron spectroscopy (XPS) spectra of the fresh samples were collected using a Specs Phoibos-150 hemispherical spectrometer equipped with a monochromatic source of $AlK\alpha$. The C1s photoelectron spectroscopy line at 284.6 eV binding energy was used as a reference [50]. The asymmetric peak shape for Niº peak was defined according to Biesinger et al., [51]. For the *in situ* reduced catalyst a reduction chamber was coupled to the spectrometer where the samples were initially heated at 500°C ($5°Cmin^{-1}$) for 30 min under a flow of He (30 $mLmin^{-1}$). Then using this same temperature they were reduced with 5% H_2/N_2, under a flow rate of 30 $mLmin^{-1}$ for 4 hours, afterwards the XPS analysis was conducted.

4.3.9.
Temperature programmed surface reaction (CO_2+H_2 - TPSR) of the methanation reaction

The temperature programmed surface reaction (TPSR) coupled to a mass spectrometer was carried out in order to identify possible intermediary species of the reaction and evaluate the activity of the catalysts. Temperature-programmed surface reaction (CO_2+H_2 -TPSR,) experiments were conducted employing a microreactor coupled to a Dycor Mass Spectrometer, Ametek Process Instruments. The samples (500 mg) were pretreated employing the same procedure described in the methodology of the CO_2-TPD. Then, they were exposed to CO_2 (20 $mLmin^{-1}$) for 30 min at room temperature. After that, the TPSR measurements were carried out heating the samples at $10°Cmin^{-1}$ up to 500°C, under pure H_2 flow (20 $mLmin^{-1}$). The fragments m/z=15, m/z=28 and m/z=44 and m/z=18, assigned to CH_4, CO, CO_2 and H_2O were continuously monitored, respectively.

4.3.10.
Temperature programmed surface reaction (CO+H$_2$ - TPSR) of the methanation reaction

Temperature-programmed surface reaction (TPSR, CO+H$_2$,) experiments were conducted employing a microreactor coupled to a Dycor Mass Spectrometer, Ametek Process Instruments. The samples (500 mg) were pretreated employing the same procedure described above. Then, they were exposed to CO (20 mLmin^{-1}) for 1 h at room temperature. After that, the TPSR measurements were carried out heating the samples at 10°Cmin^{-1} up to 500°C, under pure H$_2$ flow (20 mLmin^{-1}). The fragments m/z=15, m/z=28 and m/z=44 and m/z=18, assigned to CH$_4$, CO, CO$_2$ and H$_2$O were continuously monitored, respectively.

4.4.
Catalytic tests

4.4.1.
The methanation of CO$_2$ and CO

The catalytic tests were carried out to evaluate each catalyst during the methanation reaction of CO$_2$ and CO so as to investigate the activity, selectivity and methane yield. The reaction was carried out in a fixed bed reactor monitored by online Agilent GC-6880 gas chromatograph. Catalytic tests were carried out using 200 mg of catalyst, 80 mLmin^{-1} of flow rate, 350 °C, 1 atm, 10 %CO$_2$, 40 %H$_2$ and 50 %He (H$_2$/CO$_2$: 4/1). Another mixture comprised of 50 % of H$_2$, 220 ppm (0.022%) of CO and N$_2$ (balance) was also employed (H$_2$/CO : 3/1). The CO and CO$_2$ methanation rates were measured under differential conditions (conversion< 10%) at 350 °C and 1 atm of pressure. Long time duration tests were carried out in order to determine the degree of stability of each catalyst.

CO$_2$ conversion and selectivities are defined as following: the CO$_2$ conversion is the ratio of the CO$_2$ moles consumed to the CO$_2$ moles introduced in the feed. The definition of the selectivity to one specific compound is the ratio of the number of CO$_2$ moles consumed to synthesize this compound to the total number of CO$_2$ moles consumed.

5.
The role of the support and vacancies in the CO$_2$ methanation

5.1.
Results and discussion

5.1.1.
Chemical Composition

Table 4 shows the results of the chemical composition by X-ray fluorescence spectrometry for the determination of metallic contents (expressed in weight percentage %wt). These results are in agreement with the nominal metallic content that identifies each sample.

Table 4. Ni content of prepared catalyst via X-ray fluorescence.

Sample	%wt Ni
0.5%Ni/ZrO$_2$	0.53
2%Ni/ZrO$_2$	2.03
5%Ni/ZrO$_2$	4.80
10%Ni/ZrO$_2$	9.90
0.5%Ni/SiO$_2$	0.4
2%Ni/SiO$_2$	1.69
5%Ni/SiO$_2$	3.99
10%Ni/SiO$_2$	8.22
5%Ni/Mg(Al)O	4.52
10%Ni/Mg(Al)O	9.13

5.1.2.
Cyclohexane dehydrogenation reaction

The rate of cyclohexane dehydrogenation is shown in Table 5 and it is used in this work as an indirect measure of the Ni surface area [52]. It can be noted from Table 5 that the 10% Ni/Mg(Al)O catalyst exhibited the highest consumption rate (-rCH), which suggests a greater Ni metallic available among the other catalysts. The set of Ni/SiO$_2$ catalysts presented the least consumption rate, indicating a lower value of Ni metallic area. This result may suggest that some Ni could be agglomerated on these catalysts. It is important to highlight that 5% Ni/ZrO$_2$, 5% Ni/Mg(Al)O and 10% Ni/SiO$_2$ exhibited similar reaction rates (-rCH) suggesting that these 3 catalyst have similar Ni metallic area, which make them ideal to study the influence of the support in the CO$_2$ methanation reaction.

Table 5. Dehydrogenation reaction rates of cyclohexane for the set of catalysts.

Catalysts	-rCH mmolg$_{cat}^{-1}$min^{-1}
10% Ni/ZrO$_2$	5.7
5% Ni/ZrO$_2$	3.9
2% Ni/ZrO$_2$	2.5
0.5 Ni/ZrO$_2$	0.21
10% Ni/SiO$_2$	3.1
5% Ni/SiO$_2$	2.8
2% Ni/SiO$_2$	2.1
0.5 Ni/SiO$_2$	0.73
10% Ni/Mg(Al)O	10.3
5% Ni/Mg(Al)O	3.9

5.1.3.
N$_2$ fisissorption (BET area measurement and application of the BJH method)

Table 6 displays the specific area for the catalysts and their supports. It can be observed that the Mg(Al)O oxide presented the highest specific surface area of all the samples, followed by the SiO$_2$ oxide. The monoclinic ZrO$_2$ oxide exhibited the smallest specific area of all the supports. There is a trend to decrease the specific area after impregnation of the catalysts with high metal load, i.e., 10% Ni/SiO$_2$, 10% Ni/Mg(Al)O and 10% Ni/ZrO$_2$. This decrease may be due to the blockage of the pores of the oxide by Ni particles. Such behaviour was not observed in those catalysts with low metal content.

Table 6. Specific area (S) / m^{2}g^{-1} of catalysts and supports.

Catalysts	Specific area (S) / m^{2}g^{-1}
ZrO$_2$	67
10% Ni/ZrO$_2$	60
5% Ni/ZrO$_2$	66
2% Ni/ZrO$_2$	72
0.5 Ni/ZrO$_2$	73
SiO$_2$	78
10% Ni/SiO$_2$	67
Mg(Al)O	143
10% Ni/Mg(Al)O	134
5% Ni/Mg(Al)O	143

Figure 12 and Figure 13 display the adsorption and desorption isotherms of the three oxide supports and the Ni catalysts, 5% Ni/ZrO$_2$, 5% Ni/Mg(Al)O, and 10% Ni/SiO$_2$, respectively. According to the IUPAC classification for isotherms and hysteresis shown in Figure 14 and Figure 15, respectively, the isotherms of 5%Ni/ZrO$_2$ and ZrO$_2$ correspond to type IV [53]; characteristic of mesoporous

materials, with H1-type hysteresis which suggest well cylindrical defined pore channel [54]. The samples 10% Ni/SiO$_2$ catalyst and SiO$_2$ oxide also correspond to type V, but with H3-type hysteresis. The samples 5% Ni/Mg(Al)O and Mg(Al)O also correspond to type IV, typical of mesoporous materials, the former with H2-type of hysteresis (disordered or blocked pores) and the latter with H4-type of hysteresis suggesting narrow pores [54].
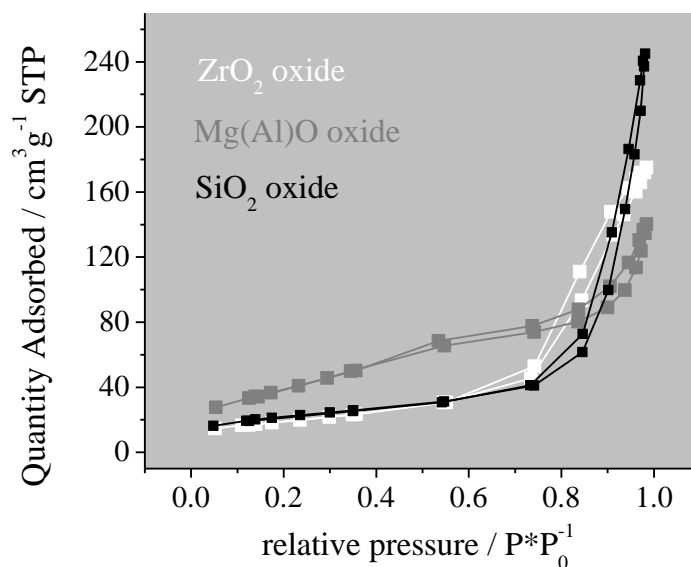
Figure 12. Adsorption isotherm of the three supports.
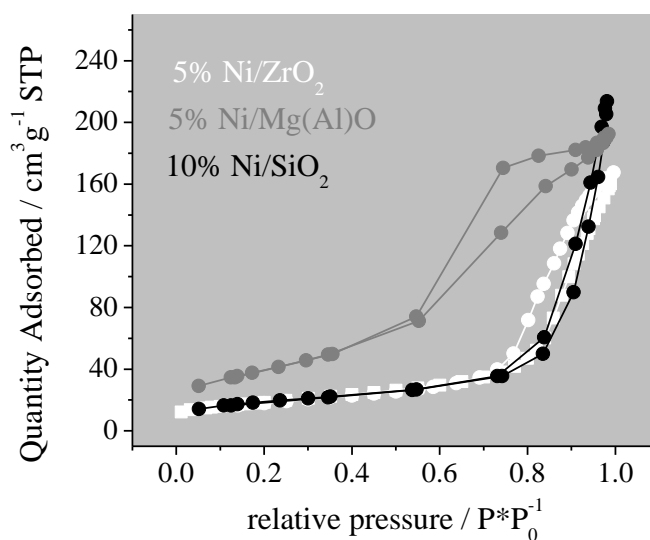
Figure 13. Adsorption isotherm of the catalysts 5% NiZrO$_2$ (white), 5% Ni/Mg(Al)O (gray) and 10% Ni/SiO$_2$ (black).
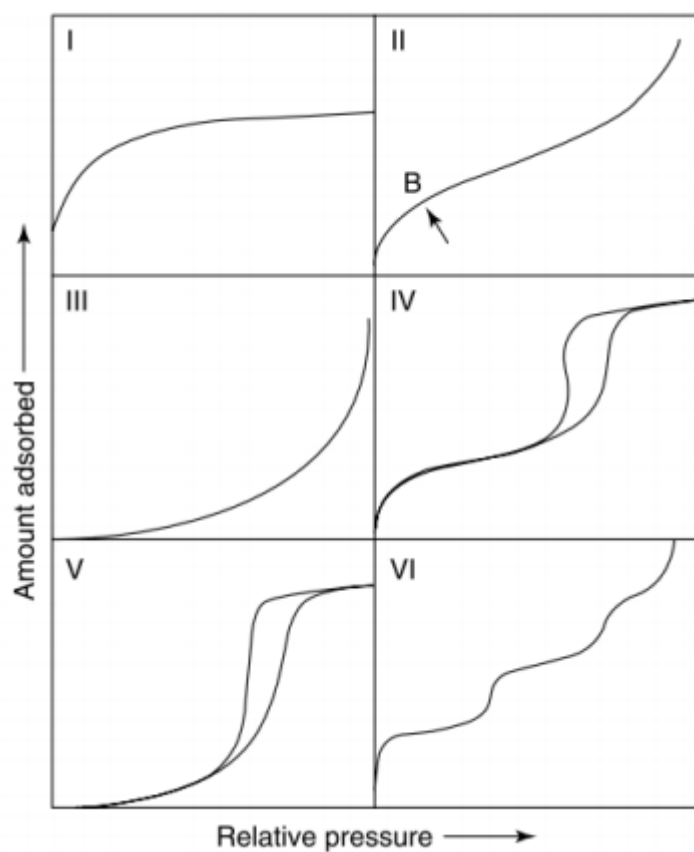
Figure 14. Types of isotherms according to IUPAC (adapted from G. Ferreira [57])
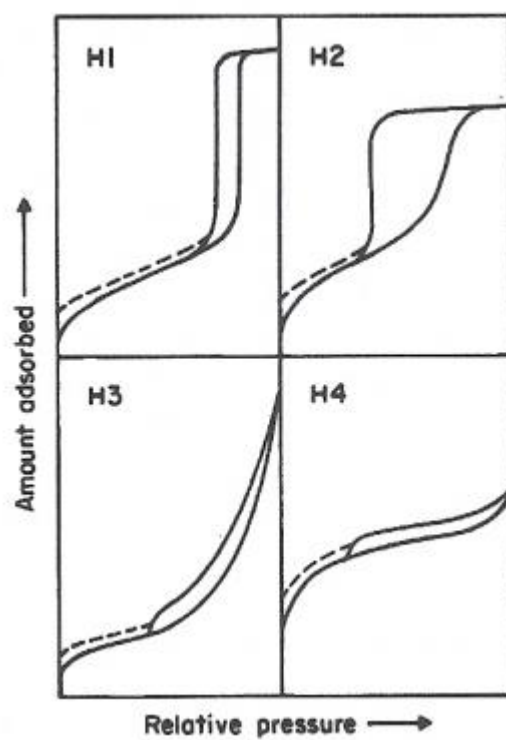
Figure 15. Hysteresis loop classifications (adapted from A. Trunschke [56]).

52

Figure 16 and Figure 17 show the pore size distribution obtained from the BJH method for all three supports and for the 5% Ni/ZrO_2, 5% Ni/Mg(Al)O and 10% Ni/SiO_2 catalysts. The ZrO_2 oxide curve exhibits a maximum around 91 Å, which is very similar to the one of 5% Ni/ZrO_2 catalyst (around 95 Å), showing that the Ni impregnation did not modify the pore diameter at all. The Mg(Al)O oxide displays a maximum of pore diameter average around 50 Å. This value is very closed to that of the 5% Ni/Mg(Al)O catalyst which exhibited a maximum at 47 Å. Finally, the SiO_2 oxide exhibited the largest pore diameter average with a maximum at 160 Å. Once this SiO_2 oxide has been impregnated with Ni, as in the case of the 10% Ni/SiO_2 the pore diameter decrease until 146 Å. From the above it can be observed that the 10% Ni/SiO_2 catalyst exhibited greater pore blockage, which is in accordance with the specific area results, since the catalyst 5% Ni/ZrO_2 and 5% Ni/Mg(Al)O did not present significant variation in the specific area after the impregnation of the oxide with Ni.

According to IUPAC porosity is classified as follows: a) microporous are pores with a diameter of less than 20 Å, b) mesoporous are pores with a diameter in the range of 20 and 500 Å, and c) macroporous are pores with a diameter greater than 500 Å. Due to the above all the samples described are considered mesoporous material.
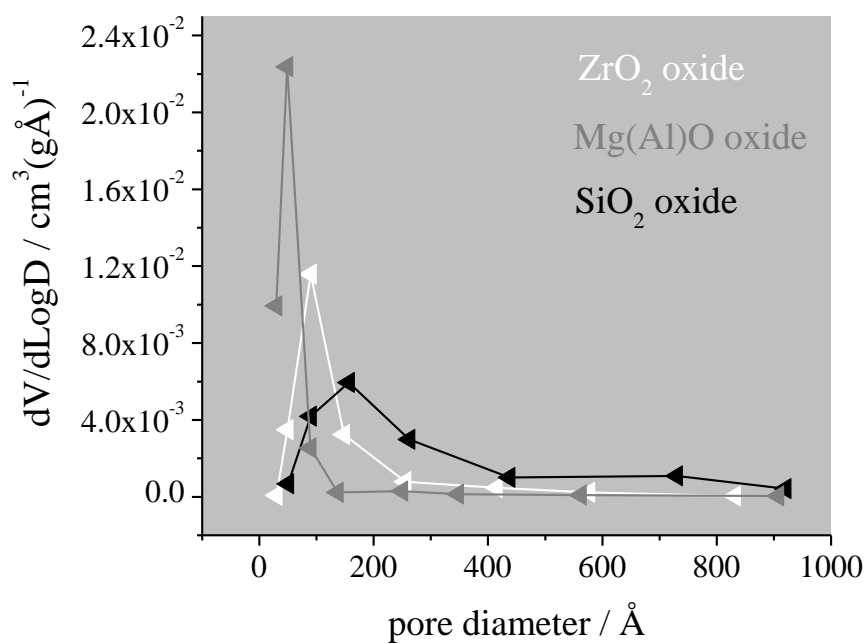
Figure 16. Pore size distribution of all supports.
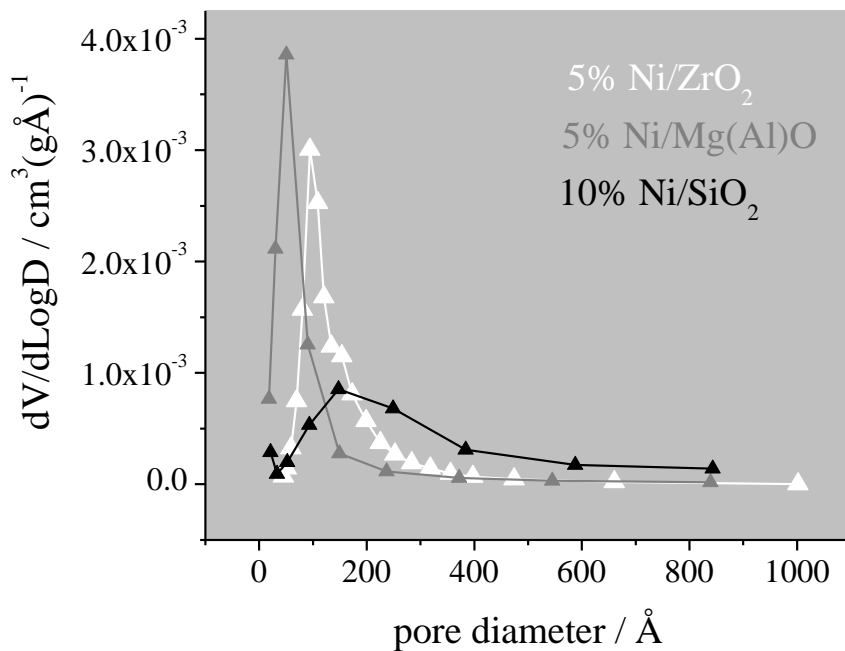
Figure 17. Pore size distribution of the catalysts 5% NiZrO$_2$ (white), 5% Ni/Mg(Al)O (gray) and 10% Ni/SiO$_2$ (black).

54

5.1.4.
Temperature programmed reduction analyses (TPR)

TPR profiles of the catalysts 10%Ni/SiO$_2$, 5%Ni/ZrO$_2$ and Ni/Mg(Al)O are shown in Figure 18. The 5%Ni/ZrO$_2$ catalyst displays a main peak in the range of 170-513 °C, which suggests the reduction of NiO to Ni^0. It also displays small shoulders at the beginning and at the end of this main peak [27]. The shoulder at the end of the main peak may suggest the reduction of Ni species that are in the ZrO$_2$ bulk (see XRD results) of the 5%Ni/ZrO$_2$ catalyst [38]. The Ni/SiO$_2$ catalyst displays a main peak between 227-400 °C related to the NiO reduction, it also exhibits two small shoulders at 435 °C and 660 °C suggesting that some NiO species still remain unreduced during reaction conditions. These NiO species are in some manner strongly bonded to the support [55], see methodology (pretreatment). Finally, the 5%Ni/Mg(Al)O catalyst exhibit a broad peak at 850 °C. This may correspond to the reduction of Ni^{2+} which has been incorporated in the mixed oxide structure Mg(Al,Ni)O [36,56], for this reason the temperature of reduction employed in the methanation of CO$_2$ for this catalyst was 700°C. It is also observed a very slightly raised curve in the range of 250-600 °C, this may be attributed to the NiO. The percentage of reduction for the 5%Ni/ZrO$_2$ and 10%Ni/SiO$_2$ samples is 93% for both systems (Table 1). The 5%Ni/Mg(Al)O presented a lower percentage of reduction (75%) due to the strong interaction with Ni^{2+} and the support forming the compound Mg(Al,Ni)O, which requires higher temperature and higher consumption of H$_2$ [56]. Table 7 displays information of the reduction characteristic of all catalyst.
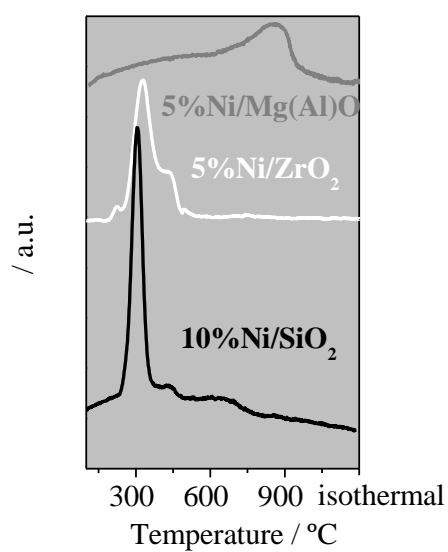
Figure 18. TPR profiles of catalysts: 10%Ni/SiO$_2$, 5%Ni/ZrO$_2$ and 5%Ni/Mg(Al)O.

Table 7. H$_2$ consumption values and percentage of reduction of catalysts 10%Ni/SiO$_2$, 5%Ni/ZrO$_2$ and 5%Ni/Mg(Al)O.

Catalyst	Theoretical H$_2$ consumption (mol)	Experimental H$_2$ consumption (mol)	% of reduction
5%Ni/ZrO$_2$	5.56E-05	5.19E-05	93
10%Ni/SiO$_2$	1.11E-04	1.03E-04	93
5%Ni/Mg(Al)O	5.19E-05	3.87E-05	75

5.1.5.
Temperature programmed desorption of CO_2 (TPD of CO_2)

Figure 19 depict the profiles of the TPD of CO_2 of the three catalysts mentioned above, and Table 8 presents the evaluated amount of weak, medium and strong basic sites. All three catalysts are able to adsorb CO_2 in different amounts. Moreover, 5%Ni/ZrO_2 catalyst shows more available sites for the adsorption of CO_2 than 5%Ni/Mg(Al)O. 10%Ni/SiO_2 adsorbs even less amounts of CO_2 than the two other catalysts. As these three catalysts exhibit the same metallic area this result can be associated with the support activity. ZrO_2 presents a strong interaction with CO_2. SiO_2 interacts weakly with CO_2 as reported by Da Silva et al. [29], therefore the presence of Ni in 10%Ni/SiO_2 catalyst is mostly responsible for the CO_2 adsorption. This catalyst shows very small amount of basic sites displayed in Table 8.

Table 8. Weak, medium and strong Basic sites (μmolCO_2gcat^{-1}) of all three catalysts (T in °C).

| Catalyst | μmol CO_2/gcat | | | |
	weak (T<130)	medium (130<T<250)	strong (T>250)	Total
10%Ni/SiO_2	2	4		6
5%Ni/Mg(Al)O	19	30	33	82
5%Ni/ZrO_2	47	73	84	204
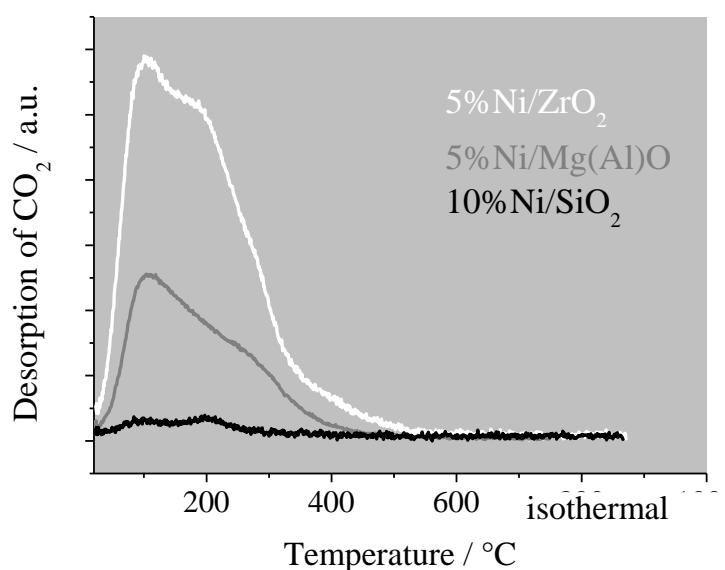
Figure 19. TPD of CO_2 spectra (m/z=44) over: 5%Ni/ZrO_2, 5%Ni/Mg(Al)O and 10%Ni/SiO_2.

5.2.1.
Catalytic Tests

The set of catalysts with different metal loads were previously tested at 350 °C in the CO_2 methanation reaction at the same residence time. All reduced with pure H_2 at 500 °C, except for Ni/Mg(Al)O system which required higher reduction temperature (700 °C), as suggested in the TPR profiles. The conversions and selectivities are displayed in Table 9**.** The conversions observed for the set of Ni/ZrO_2 catalysts are higher than the ones exhibited for Ni/Mg(Al)O and Ni/SiO_2. The Ni/ZrO_2 catalysts exhibited around 98% of selectivity for methane with almost no CO formation. The Ni/Mg(Al)O catalysts exhibited lower activity when compared with Ni/ZrO_2 with the same metal load. Its selectivity for CH_4 is also below that registered for the Ni/ZrO_2 systems, but its selectivity for CO is higher. Finally, Ni/SiO_2 catalysts exhibited the lowest activity compared for the same Ni load, with low selectivity for CH_4 and high selectivity for CO.

Comparing the three catalysts with the same Ni metallic area (grey lines), it can be observed that the ZrO_2 is the most active (higher selectivity) whereas the SiO_2 based catalyst shows the lowest selectivity towards methane.

58

Table 9. Catalytic test (200 mg, 80 mLmin^{-1}, 350 °C, 1atm and H$_2$/CO$_2$:1/4) for a set of samples in the CO$_2$ methanation reaction.

Catalysts	Conversion %	S$_{methane (TCD)}$	S$_{CO \%}$
10% Ni/ZrO$_2$	71.5	98.6	1.4
5% Ni/ZrO$_2$	46.3	98.5	1.5
2% Ni/ZrO$_2$	32.9	97	3
0.5% Ni/ZrO$_2$	12.1	97.9	2.1
10% Ni/SiO$_2$	24	47	53
5% Ni/SiO$_2$	19.2	35	65
2% Ni/SiO$_2$	13.7	11.5	88.5
0.5 Ni/SiO$_2$	5.5	5.3	94.7
10% Ni/Mg(Al)O	40.4	95.5	4.5
5% Ni/Mg(Al)O	25.1	74.6	25.4

Table 10 displays the catalytic tests for 10% Ni/SiO$_2$, 5% Ni/ZrO$_2$, and 5% Ni/Mg(Al)O catalysts (the ones with the same Ni metallic area) in the methanation of CO as well as the consumption rate of CO. The 5% Ni/ZrO$_2$ catalyst is the most active whereas the selectivity to CH$_4$ is similar for the three catalysts. According to some authors the rate limiting step is the C-O dissociation of CO or formate species.

Table 10. Catalytic tests (200 mg, 80 mLmin^{-1}, 350 °C, 1 atm and H$_2$/CO:1/3) and CO consumption rate (at 350°C, 1 atm, employing differential conditions (conversion <10%)) for a set of selected of samples in the CO methanation reaction.

Catalysts	Conversion %	S$_{methane (TCD)}$ %	-r$_{CO}$ / mmolg$_{cat}^{-1}$min^{-1}
10% Ni/SiO$_2$	12	85.6	39
5% Ni/ZrO$_2$	97.7	80.5	197
5% Ni/Mg(Al)O	61.2	76.1	77

Table 11 presents the reaction rates of the methanation of CO_2 for all the set of catalysts at 350 °C, 1 atm, employing differential conditions (conversions <10%). It can be observed that the 10%Ni/ZrO$_2$ is the most active catalyst of all the set, followed by the 10%Ni/Mg(Al)O catalyst. The 5%Ni/ZrO$_2$ catalyst occupies the third position in relationship to its activity. Moreover, it is interesting to observe that the catalysts 5%Ni/SiO$_2$ and 5%Ni/Mg(Al)O exhibit similar CO_2 consumption rate, but the latter exhibited higher methane formation rate. These results are in line with the ones of Table 9 and Table 10.

Table 11. Reaction rate (-rCO$_2$) (at 350 °C, 1atm, employing differential conditions (conversion <10%)), methane rate of formation (rCH$_4$) and CO rate of formation (rCO) for all set of catalysts

Catalysts	-rCO$_2$ mmolg$_{cat}^{-1}$min^{-1}	rCH$_4$ mmolg$_{cat}^{-1}$min$^-$	rCO mmolg$_{cat}^{-1}$min$^-$
10% Ni/ZrO$_2$	150	148	2
5% Ni/ZrO$_2$	110	103	7
2% Ni/ZrO$_2$	39	38	1
0.5 Ni/ZrO$_2$	14	13	1
--			
10% Ni/SiO$_2$	62	14	48
5% Ni/SiO$_2$	36	13	23
2% Ni/SiO$_2$	19	2	17
0.5 Ni/SiO$_2$	4	0	4
--			
10% Ni/Mg(Al)O	127	121	6
5% Ni/Mg(Al)O	40	23	17

From this set of catalytic systems we have selected some of them with the same metallic surface area (according to the rate of cyclohexane dehydrogenation) for a deeper study, they are **5% Ni/ZrO$_2$, 10% Ni/SiO$_2$ and 5%Ni/Mg(Al)O** which were renamed as **Ni/ZrO$_2$, Ni/SiO$_2$ and Ni/Mg(Al)O,** respectively**.** These selected catalysts are discussed throughout the rest of the present chapter.

Figure 20 presents the CO_2 conversion as a function of temperature for the methanation of CO_2. The Ni/ZrO$_2$ definitely exhibits higher conversions of CO_2 when compared with the Ni/Mg(Al)O and Ni/SiO$_2$ systems in the same range of temperature, The Ni/Mg(Al)O reveals almost the same conversion as the Ni/SiO$_2$ in the range of temperature of 230-360 °C. Above this range the Ni/Mg(Al)O starts to increase its conversion drastically in comparison with that verified for Ni/SiO$_2$.

Figure 21 shows the selectivity for methane and CO in the same range of temperature. It can be observed that Ni/ZrO$_2$ catalyst has almost 98% of selectivity for methane in the entire range of temperature evaluated, followed by the Ni/Mg(Al)O catalyst which exhibits increasing selectivity for methane ranging from 60% at 325 °C to 97% at 420 °C. The Ni/SiO$_2$ shows the lowest methane selectivity of all the systems being evaluated; it shows 42% in the range temperature of 270-330 °C. Then it starts increasing gradually until it reaches 70% at 420 °C.

.
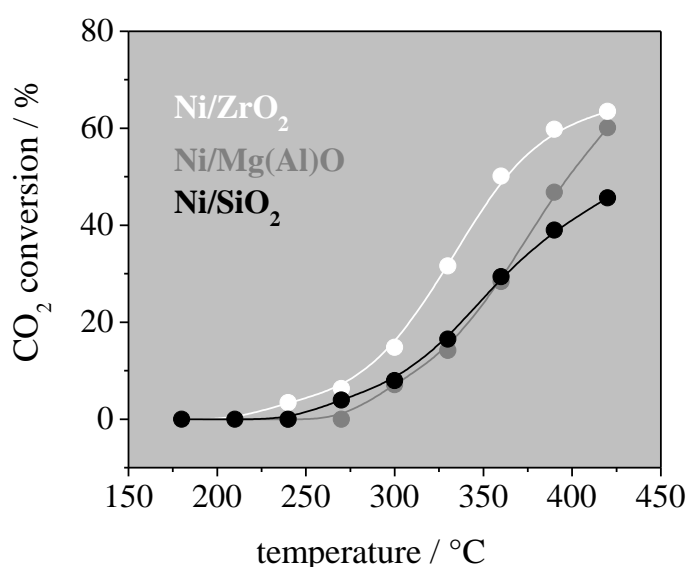
Figure 20. CO_2 conversion versus temperature of the catalysts NiZrO$_2$ (white), Ni/Mg(Al)O (gray) and Ni/SiO$_2$ (black).
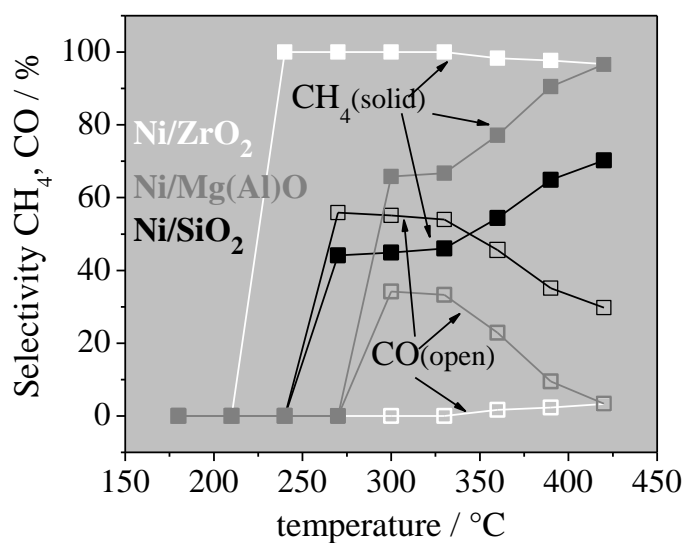
Figure 21. Selectivity for CH_4 and CO versus temperature of the catalysts $NiZrO_2$ (white), $Ni/Mg(Al)O$ (gray) and Ni/SiO_2 (black).

5.2.2.
Stability tests

The activity stability of the Ni/ZrO_2, $Ni/Mg(Al)O$ and Ni/SiO_2 catalysts at 350 °C is shown in Figure 22. It is observed that CO_2 conversion is definitely stable after 14 hours of time on stream for all catalyst as well as the CH_4 and CO selectivity shown in Figure 23.

62
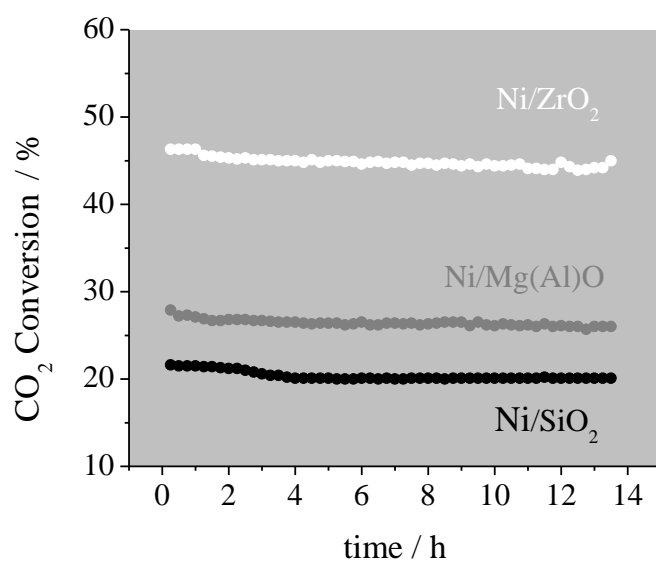
Figure 22. Catalytic stability of the activity of Ni/ZrO$_2$ (white), Ni/Mg(Al)O (gray) and Ni/SiO$_2$ (black) catalysts for CO$_2$ methanation at 350 °C, 200 mg, H$_2$/CO$_2$ 4:1, 80 mLmin^{-1} and 1 atm.
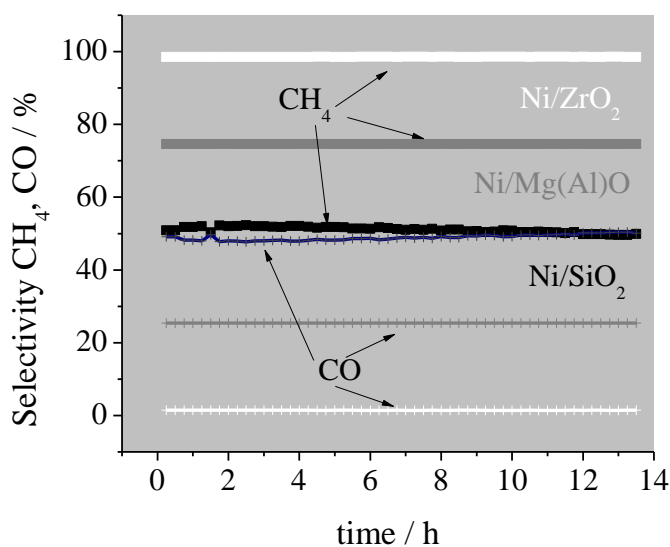
Figure 23. Catalytic stability of the CH$_4$ and CO selectivity of Ni/ZrO$_2$ (white), Ni/Mg(Al)O (gray) and Ni/SiO$_2$ (black) catalysts for CO$_2$ methanation at 350 °C, 200 mg, H$_2$/CO$_2$ 4:1, 80 mLmin^{-1} and 1 atm.

5.3.1.
Electron paramagnetic resonance (EPR)

Figure 24 shows the EPR spectra of the ZrO_2 and Mg(Al)O reduced supports. The ZrO_2 spectrum shows paramagnetic signals related to Zr^{+3} (g=1.978 and 1.963). Which corresponds to coordinately unsaturated site (cus) and are considered acid sites. Five equally spaced lines at g = 2 region are probably due to Mn^{+2} which may be an impurity of this oxide. A narrow signal at g =2.00 and a broad one with g = 2.05 in Mg(Al)O spectrum as well as g=2.06 for ZrO_2 spectrum can be associated with isolated vacancies (considered basic sites) and ferromagnetic ordering, respectively [36,57-58]. The area of the spectra was calculated by deconvolution in lorentz lines. It is worth stressing that the ZrO_2 spectrum component area related to the vacancies is 1.6 times the one of the Mg(Al)O support. These results show a greater presence of vacancies for the ZrO_2 support when compared with Mg(Al)O support.
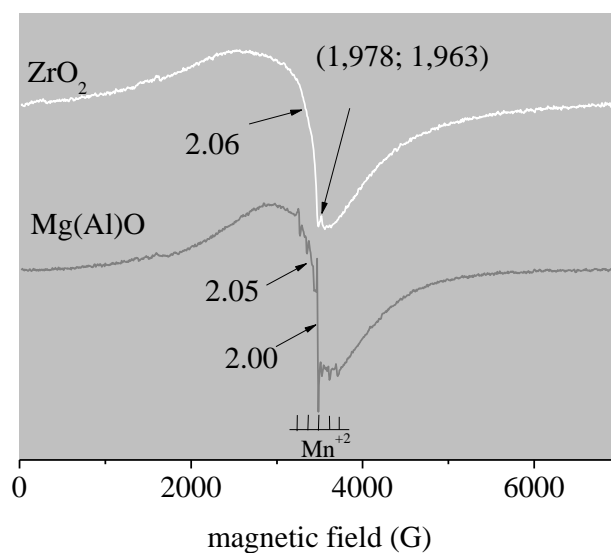
Figure 24. EPR spectrum of ZrO_2 and Mg(Al)O supports.

5.3.2.
X-ray diffraction

Figure 25 displays the XRD patterns of the reduced-passivated catalysts. The peaks at 44.63°, 52.00° and 76.66° of the Ni/ZrO_2 catalysts are attributed to the diffractions of the (111), (002) and (022) crystal planes of metallic Ni (CIF 43397-ICSD), respectively. The reflexions at 28.44°, 31.61°, 34.28°, 35.5°, 41.1°, 45.12°, 50.6° are attributed to the diffractions planes (1-1-1), (111), (002), (200), (102) and (1-2-2) of the monoclinic zirconia phase (CIF 18190-ICSD), respectively, while the peaks at 30.52°, 50.12°, 50.6° and 60.53° are related to the diffraction planes (011), (112), (020) and (211) of the tetragonal zirconia phase (CIF 68781 ICSD), respectively. It was verified via Rietveld refinement (Table 12) method using Topas software that for Ni/ZrO_2 reduced-pasivated catalyst, some Ni^{2+} ions were inside the zirconia lattice replacing some Zr^{4+} (1% of Ni^{2+} occupancy in the ZrO_2 lattice), the small difference between the ionic radius of the Ni^{2+} (0.069 nm) and Zr^{4+} (0.084 nm) facilitates the substitution of ions in the ZrO_2 lattice [37]. Moreover, the difference in charges of Ni^{2+} and Zr^{4+} results in the creation of oxygen vacancies as punctual defects [59,60]. Table 12 also shows the composition of the catalyst. It can be observed that the percentage of Ni metallic and NiO, together are consistent with the fluorescence X-ray analysis.

The XRD pattern for Ni/Mg(Al)O reduced catalyst is also shown in Figure 25. It was difficult to distinguish the peaks for metallic Ni from the support due to superposition, yet the Rietveld fitting allowed the proper separation (Table 12). The support of the Ni/Mg(Al)O catalyst presented peaks at 37.09°, 43.12° and 62.02°, 75.50° and 79.28° attributed to diffraction planes (111), (002), (022), (311) and (222), of the periclase phase (ICSD 159374), respectively, formed from the mixed oxide Mg(Al)O after calcination at 500°C. The cubic form of the magnesium oxide MgO periclase-type structure [61] presents very similar reflection angles with a variation of 0.6° to those of the mixed oxide Mg(Al)O. This variation may be attributed to the substitution of Mg^{2+} ions (ionic radius = 0.072 nm) by Al^{+3} (ionic radius = 0.054 nm), The Rietveld refinement suggests the presence of Al^{3+} ions inside the structure of the reduced Ni/Mg(Al)O catalyst

[36]. This substitution gives rise to the solid solution of Mg(Al)O generating Mg^{2+} vacancies. The anionic vacancies of Ni/Mg(Al)O catalyst might be promoted by reduction treatment at 700°C. It is important to mention that no Ni^{+2} ions were found inside the Mg(Al)O lattice, reflecting the same behavior of the Ni/ZrO$_2$ (see below) reduced catalyst where some Ni^{+2} ions tend to exit the Mg(Al)O lattice during the reduction pretreatment. Table 12 also shows the composition of phases for the Ni/Mg(Al)O catalyst.

Figure 26 displays the XRD patterns of the calcined catalysts. It was possible to verify the presence of the NiO phase on the Ni/ZrO$_2$ catalyst surface due to the reflection peaks at 37.19°, 43.35°, 62.98°, 75.48°, 79.44° and 79.81° corresponding to planes (003), (012), (110), (015), (006) and (202) (CIF 92128 ICSD), respectively. It was verified via Rietveld refinement, that Ni^{+2} ions on the Ni/ZrO$_2$ oxidized catalyst entered the ZrO$_2$ lattice in a greater amount than that verified for the Ni/ZrO$_2$ reduced catalyst, this result may suggest that the oxygen vacancies are created after the calcination of the catalyst. The reduction pretreatment favors the migration of Ni^{+2} to the ZrO$_2$ surface, where it is reduced to Ni^0 leaves the ZrO$_2$ lattice, and is available for the reaction. Some of the oxygen vacancies are still present after the reduction process, because not all Ni^{+2} exited the ZrO$_2$ lattice. These oxygen vacancies may play an important role in the reaction to receive and release oxygen, enhancing the oxidative-reductive properties of the catalyst.

The XRD pattern of the calcinated catalyst of Ni/Mg(Al)O is also shown in Figure 26. NiO was not detected in the XRD pattern. It is believed that all Ni^{+2} was incorporated in the (Mg,Al)O lattice, forming a solid solution (Mg,Al,Ni)O as suggested by Rodrigues et al. [36]. According to the Rietveld refinement (Table 12) there exist about 3.60 % Ni^{2+} ions (0.036 of Ni^{2+} occupancy factor) incorporated in the MgO periclase structure, Al^{3+} ions were also encountered inside this structure of the calcinated Ni/Mg(Al)O catalyst.

The Ni/SiO$_2$ reduced catalyst exhibits a very broad peak at 21.93° which is characteristic of the amorphous SiO$_2$. The metallic Ni phase in this catalyst showed three peaks at 44.76°, 51.88° and 76.35° attributed to the diffraction from planes (111), (002) and (022), respectively (CIF 43397-ICSD).
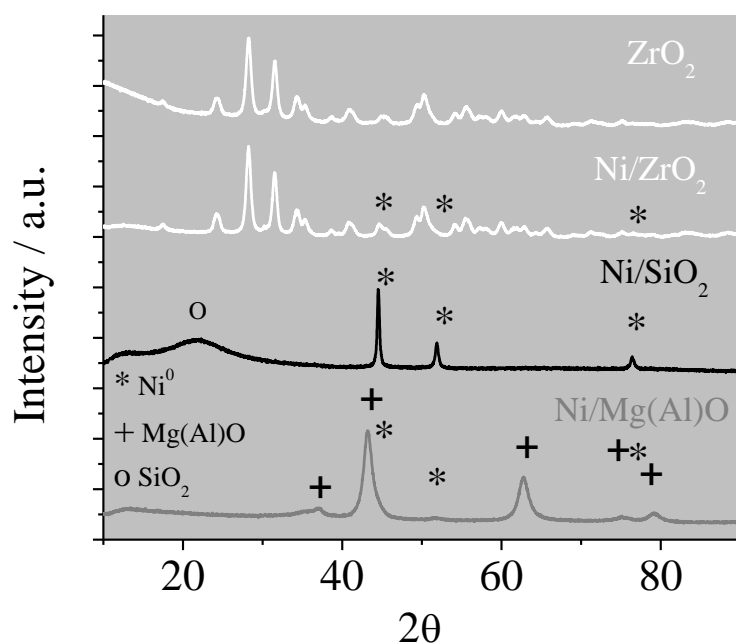
Figure 25. XRD patterns of the reduced-passivated catalysts (Ni/ZrO$_2$, Ni/Mg(Al)O and Ni/SiO$_2$) and support (ZrO$_2$) reduced-passivated.
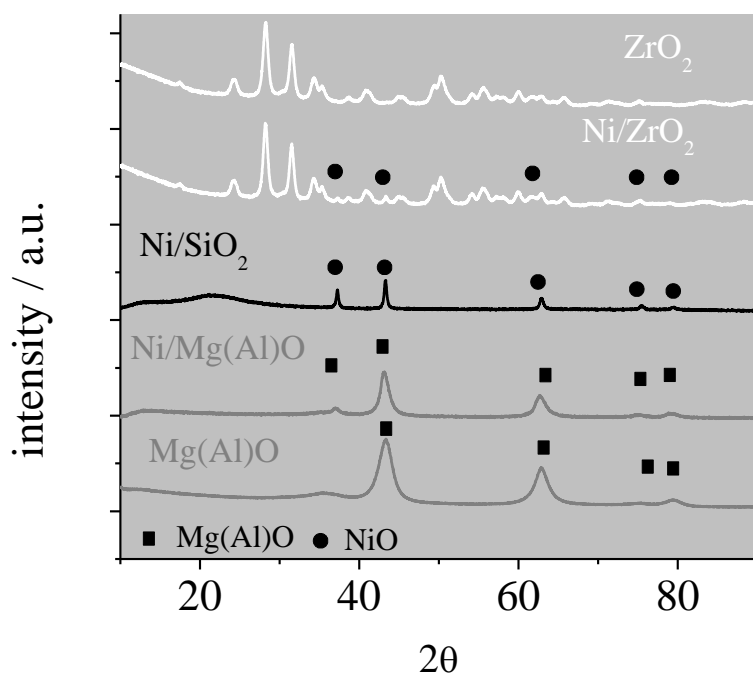
Figure 26. XRD patterns of the synthesized catalysts (Ni/ZrO$_2$, Ni/Mg(Al)O and Ni/SiO$_2$) and supports (ZrO$_2$ and Mg(Al)O) after calcination.

Table 12. Crystallographic parameters determined by Rietveld Refinement of the oxidized and reduced-passivated catalysts.

line	catalysts / column		Ni/ZrO$_2$		Ni/Mg(Al)O		ZrO$_2$	Mg(Al)O
			oxidized	reduced	oxidized	reduced	oxidized	oxidized
			1	**2**	**3**	**4**	**5**	**6**
		MONOCLINIC PHASE - *m*-ZrO$_2$						
1	lattice parameters /Å	a	5.1392	5.1425			5.1402	
2		b	5.1959	5.2001			5.1960	
3		c	5.3078	5.3122			5.3086	
4		β / º	99.2011	99.2210			99.2394	
5	occupancy	**O^{-2}(1)**	0.9190	0.9381			1.0000	
		O^{-2}(2)	0.9653	0.9894			1.0000	
6		Zr^{+4}	0.9700	0.9900			1.000	
7		Ni^{+2}	0.0346	0.0106				
		MgO PHASE						
8	lattice parameters / Å	a			4.2265	4.1868		4.1800
9	occupancy	Mg^{+2}			0.4427	0.6000		0.8900

10		Al^{+3}			0.5213	0.4000		0.1100
11		O^{-2} (1)			1.0000	1.000		1.0000
12		Ni^{+2}			0.0360	0.000		
		PHASE / wt.%						
13		m-ZrO_2	92.2	92.5			96.9	
14	phase / wt.%	t-ZrO_2	2.3	2.1			3.1	
15		Ni^0	0	4.2	0	2.6		
16		NiO	5.4	1.2	0	0		
17		MgO	----	-----	99.14	97.20		99.9
18		Al_2O_3			0.86	0.30		0.1
		CELL VOLUME / Å^3						
19		m-ZrO_2	139.91	140.22			139.95	
20	cell volume / Å^3	t-ZrO_2	67.12	67.40			67.00	
21		Ni^0	-------	43.65		43.95		
22		NiO	54.40	55.00				
23		MgO			75.50	73.39		73.04
24	GOF		1.21	1.35	1.34	1.60	1.36	1.35

5.3.3.
X-ray Photoelectron Spectroscopy (XPS)

Figure 27 displays the Ni $2p_{3/2}$ spectra obtained for all three oxidized catalysts showing three different components. Table 13 shows the binding energy and atomic ratios for the observed species.
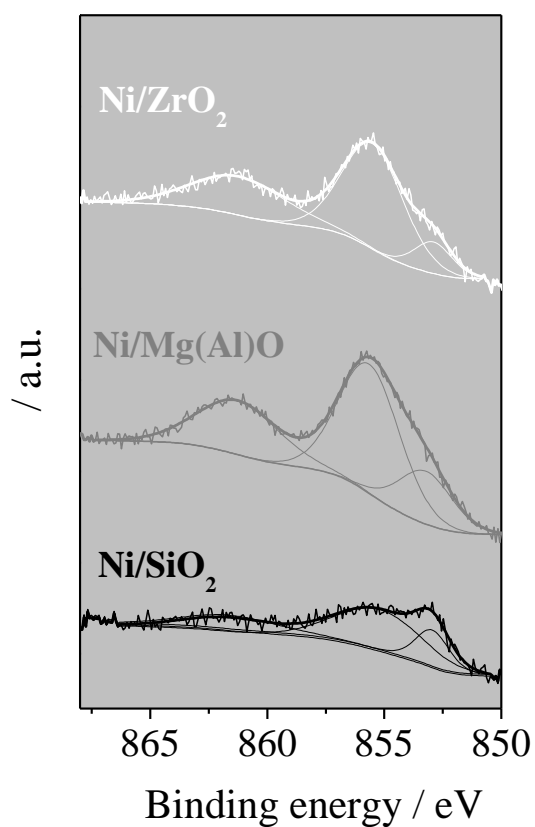
Figure 27. XPS spectra for the $Ni2p_{3/2}$ region of catalysts Ni/ZrO_2, $Ni/Mg(Al)O$ and Ni/SiO_2.

Table 13. Binding energy of Ni2p3/2 (eV) and Ni/Si, Ni/Zr and Ni/Mg atomic ratios obtained by XPS of the oxidized samples.

Catalyst	Binding energy (eV)		Atomic ratios		
	Ni2p$_{3/2}$	species	Ni/Si	Ni/Mg	Ni/Zr
Ni/SiO$_2$	852.9	NiO [50]	0.008	-	-
	855.2	Si-O-Ni			
	862	satellite			
Ni/Mg(Al)O	853.2	NiO [50]	-	0.03	-
	855.6	Ni^{2+} in the MgO lattice [36]			
	861.5	satellite			
Ni/ZrO$_2$	852.9	NiO [50]	-	-	0.027
	855.5	Ni^{2+} in the ZrO2 lattice [62]			
	861.6	satellite			

Ni/ZrO$_2$ catalyst presents a component at 852.9 eV, related to NiO [50]. The Ni/ZrO$_2$ catalyst displays a second and third component at 855.5 eV and 861.6 eV, respectively, the former can be associated with insertion of Ni into ZrO$_2$ lattice [62] and the latter signal at 861.6 eV corresponds to its satellite [63].

The Ni/Mg(Al)O presents a component at 853.2 eV associated to NiO [50], a second and third component is observed at 855.6 eV and 861.5 eV, respectively, the former is associated with the Ni^{2+} inside the MgO lattice whereas the latter is its satellite [36], this result is in accordance with XRD refinement previously discussed.

The Ni 2p3/2 XPS spectra for Ni/SiO$_2$ catalyst presented low intensity of Ni peaks, it can be suggested that some Ni is agglomerated and/or inside the pores of the SiO$_2$ as reported by Umegaki et al. [64]. This catalyst shows a component at 852.9 eV. This binding energy matches exactly with that of the Ni/ZrO$_2$ catalyst indicating the presence of NiO. A second and third peaks are observed at 855.2 eV and 862.0 eV, the former can be associated with the presence of NiO (Ni^{+2}) that can be partially bonded to SiO$_2$ and the latter is its satellite, respectively. Umegaki et al., studied the XPS spectra of hollow Ni/SiO$_2$ nanosphere catalyst and suggested that the presence of partial oxidized Ni atoms with binding energy of 855.7 eV may be related to the interaction bond Si-O-Ni [64].

71

Table 13 also shows the atomic ratios of Ni/Si, Ni/Zr and Ni/Mg. It can be inferred that Ni/ZrO$_2$ and Ni/Mg(Al)O present similar Ni atomic concentration on the surface, this result agrees with rate of cyclohexane dehydrogenation which showed similar values between the metallic areas of the catalysts. Ni/SiO$_2$ catalyst exhibited a lower Ni/Si ratio when compared with the Ni/Zr and Ni/Mg ratios, this might be attributed to the preferential inclusion of Ni in the pores of SiO$_2$ (heterogeneous distribution between internal and external area) as mentioned above [64]. When nickel reduces, it exits the lattice (in the case of ZrO$_2$ and Mg(Al)O supports) and also breaks the bond with SiO$_2$. Thereby, taking into account for the Ni/Si ratio calculation all Ni accounted is correct since the cyclohexane dehydrogenation analyses requires reduced catalysts.

5.3.4.
Temperature programmed surface reaction (TPSR, CO$_2$+H$_2$) of the methanation reaction (coupled to a mass spectrometer)

Figure 28, Figure 29 and   Figure 30 display the TPSR of CO$_2$ + H$_2$ of the Ni/ZrO$_2$, Ni/Mg(Al)O and Ni/SiO$_2$, respectively. Comparing Figure 28   and Figure 29 it can be verified that the spectra among them are very similar with the exception of water desorption. Ni/ZrO$_2$ generates H$_2$O at much lower temperatures than Ni/Mg(Al)O.

This reaction probably occurs according to the following steps (Figure 31): firstly, CO$_2$ is adsorbed; then, it displaces one of its O atoms in the anionic vacancies of the support generating CO. After that, H$_2$ is dissociated on the metal. The H species spillover to the oxide and eliminate the O and reduce the catalyst producing H$_2$O, recovering the vacancies [65,66]. Then the CO interacts with the cus-oxygen vacancy pair. It is dissociated to C which then is hydrogenated to CH$_4$.

The TPSR - CO$_2$+H$_2$ spectra show that the methane bands are similar (intensity and maximun temperature) for both catalyst and the H$_2$O spectra very different. Suggesting that CO dissociation   (limiting step of CO$_2$ methanation, see literature review section 2.8) occurs on anionic vacancies and cus, (coordinative unsaturated sites) (see EPR spectra). It can be inferred that the

elimination of water and recovery of vacancies is more difficult for the Ni/Mg(Al)O catalyst, which might impacts its activity and selectivity in the reaction of interest. In addition the number of anionic vacancies is lower for the Ni/Mg(Al)O catalyst compared to that of Ni/ZrO_2 catalyst. See the catalytic test data above and the EPR results. Ni/ZrO_2 is able to absorb more CO_2 (TPD of CO_2) which is favorable for the reaction.

Figure 30 shows a very low signal of CH_4 which may be attributed to the Ni particles, since SiO_2 is considered an inert support.
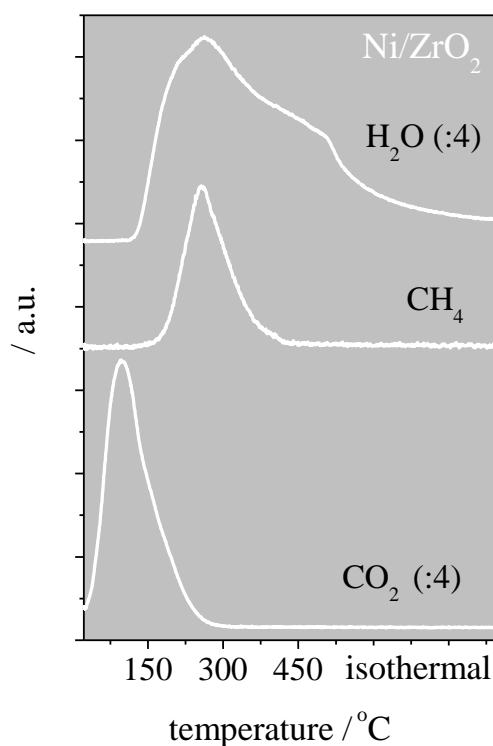
Figure 28. TPSR of CO_2 spectra over Ni/ZrO_2.
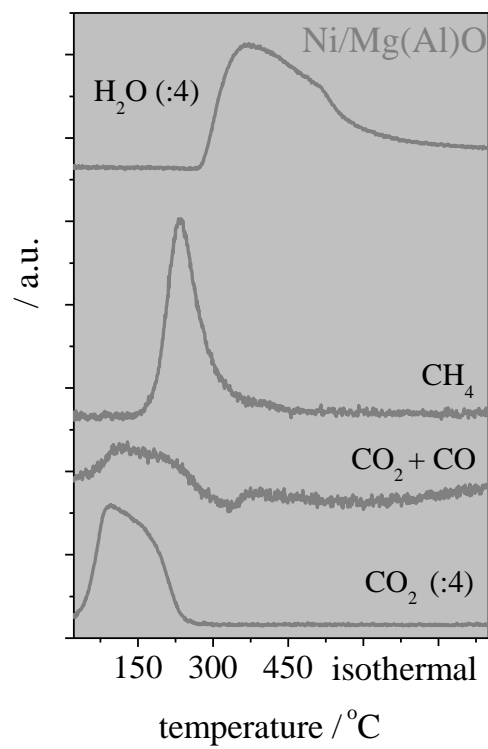
Figure 29. TPSR of CO_2 spectra over Ni/Mg(Al)O.
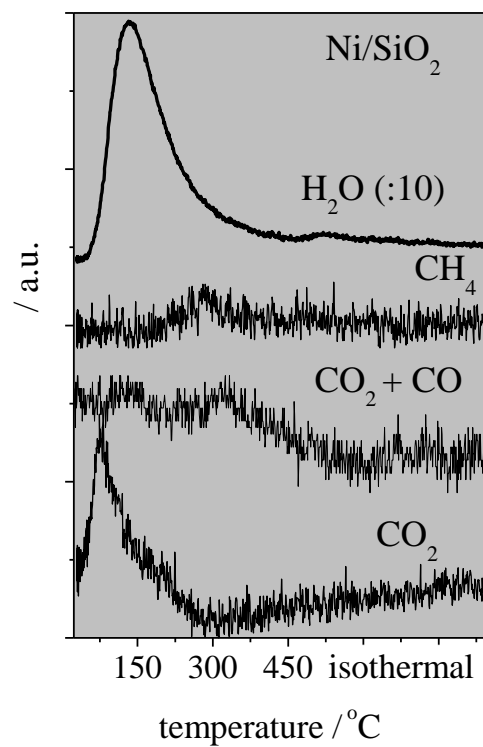
Figure 30. TPSR of CO_2 spectra over Ni/SiO_2.
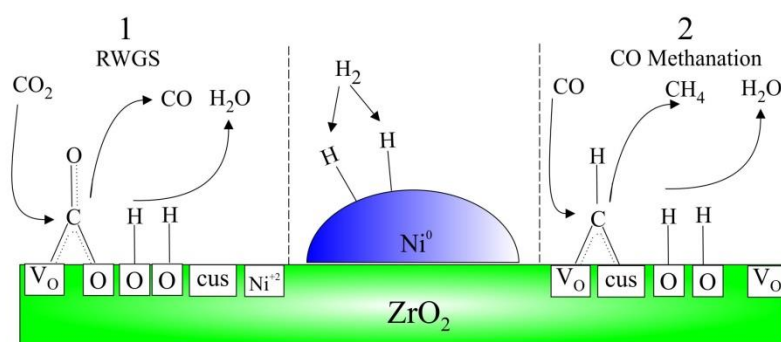
Figure 31. A probable mechanism of CO_2 methanation on Ni/ZrO_2 catalyst.

75

5.3.5.
Temperature programmed surface reaction (TPSR, CO+H$_2$) of the methanation reaction (coupled to a mass spectrometer)

Figure 32 displays the TPSR of the methanation reaction of CO on Ni/ZrO$_2$, Ni/Mg(Al)O and Ni/SiO$_2$ catalysts.
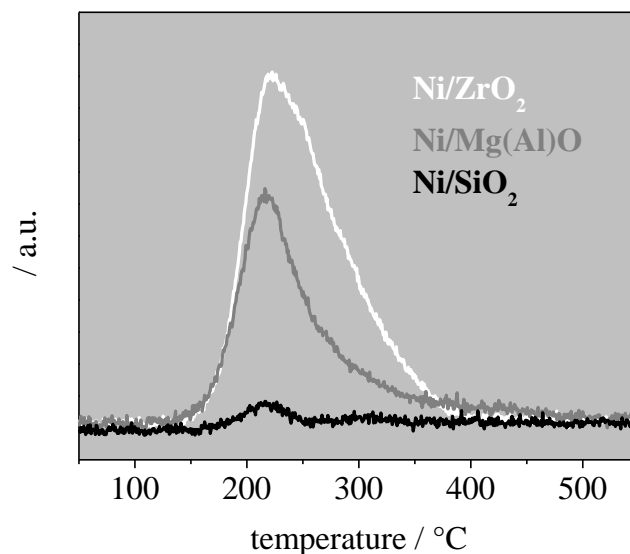
Figure 32. TPSR of CO spectra for methane (m/z=15) over: Ni/ZrO$_2$, Ni/Mg(Al)O and Ni/SiO$_2$.

It can be observed that Ni/ZrO$_2$ catalyst generates more methane than Ni/Mg(Al)O and Ni/SiO$_2$ systems. This result agrees with reaction rate of the CO methanation reaction (shown in Table 10) which exhibits a higher value for the Ni/ZrO$_2$ catalyst. The Ni/SiO$_2$ catalyst shows one small peak which can only be assigned to the Ni sites. This result indicates that the role of Ni in the methanation of CO$_2$ on the ZrO$_2$ and Mg(Al)O based catalyst is more related to the H$_2$ dissociation than the methanation itself. Considering the fact that these three catalysts have been prepared to have the same metallic area and that SiO$_2$ is an inert support without oxygen vacancies, it can be suggested that the intense broad peaks in the Ni/ZrO$_2$ and Ni/Mg(Al)O catalysts are associated with the sites available on the support. Oxygen vacancies and cus pairs on the ZrO$_2$ and Mg(Al)O supports might be responsible for the CO adsorption and transformation

to CH_4 [33,35,67]. Further, the EPR analysis reveals a higher concentration of oxygen vacancies for the ZrO_2 support than that from the $Mg(Al)O$ support, consistent with the larger generation of CH_4 observed on the Ni/ZrO_2 catalyst . Considering the two step mechanism involving CO formation, this fact demonstrates that Ni/ZrO_2 catalyst is more active in the second step of the reaction where CO hydrogenates to CH_4, this fact represent an advantage for the Ni/ZrO_2 catalyst compared to the $Ni/Mg(Al)O$ and Ni/SiO_2 systems, since it is well accepted that the CO dissociation is the rate-determining step of the CO_2 methanation reaction [10,41,45,68]. It can be suggested that the pair oxygen vacancies − cus are facilitating the rupture of the CO bond, thereby, the rate of CH_4 formation is enhanced.

5.4.1.
Conclusion to chapter 5

The high activity of Ni/ZrO_2 catalyst toward the methanation of CO_2 is related to the presence of oxygen vacancies on the ZrO_2 support. XRD analysis showed that some Ni is in the lattice of the ZrO_2 support generating O vacancies, also confirmed by EPR results. Indeed, EPR data showed a greater concentration of O vacancies in the ZrO_2 support than in $Mg(Al)O$ support. Moreover, the higher reductibility as shown by the TPSR of $CO_2 + H_2$ analysis also improves the catalytic behavior of the ZrO_2 based catalyst.

The oxygen vacancies seem to be very relevant for the methanation of CO_2. Thus, in the following chapter a catalyst with a higher concentration of oxygen vacancies was prepared in order prove the fact described above.

.

6.

The role of oxygen vacancies in the CO_2 methanation employing Ni/ZrO_2 doped with Ca

6.1.
Introduction

The production of synthetic natural gas (SNG) from CO_2 and H_2, the latter generated from H_2O electrolysis, is a very promising CO_2 utilization as raw material [2,69]. Methane is an energy carrier employed in many countries in the transport sector and industry. Moreover, SNG has been proposed for the storage of intermittent energy, as for instance, the solar and wind sources. Guilera et al. [69] analyzing the parameters that affect the economic feasibility of the SNG synthesis for energy storage verified that the performance of the methanation catalyst is one of the most relevant topics.

Two CO_2 methanation mechanisms have been proposed when the supports of the catalysts interact with CO_2. The successive hydrogenation of CO_2 to CH_4 is the first one. Carbonates, formates and methoxy species are intermediates of this mechanism [1,2,17,35]. The second one can be described as following: firstly, CO_2 is reduced to CO by the RWGS and, the second step is the hydrogenation of CO to CH_4. [1,17,45,70,71].

Ashok et al. [35] have studied the CO_2 methanation over Ni supported on $Ce_xZr_{1-x}O_2$. They suggested that Ni^{2+} is incorporated into the mixed oxide lattice generating oxygen vacancies which enhance the adsorption of oxygenate species. Takano et al. [32] employing Ni/ZrO_2 showed that the isomorphic substitution of Zr^{4+} by the Sm^{3+}, Y^{3+}, Ni^{2+} an Ca^{2+} cations in the ZrO_2 lattice improves the performance of the catalyst due to the generation of oxygen vacancies. These species increase the CO_2 adsorption and also the catalytic activity. Wang et al. [25] using Ru/CeO_2 and the steady-state isotope transient kinetic analysis observed that the oxygen vacancies of CeO_2 are active sites of the CO_2

methanation rate-determinant step, i.e., the formate dissociation which generates methoxide species. On the other hand, Jia. et al [33] employing plasma in the Ni/ZrO$_2$ catalyst preparation suggested that the main role of the oxygen vacancies is associated with the CO$_2$ adsorption and activation. Recently, J. Lin et al. [34], employing mesoporous Ni/Al$_2$O$_3$-ZrO$_2$ catalysts prepared by the sol-gel method suggested that both Ni and oxygen vacancies play a crucial role in the improvement of the catalytic activity and CH$_4$ selectivity. These authors suggested that the CO$_2$ and CO dissociations occur on oxygen vacancies. According to the literature, oxygen vacancies are very relevant for the CO$_2$ methanation. Although there are many interesting propositions about the main role of the oxygen vacancies in the CO$_2$ methanation, there is no a real consensus about this subject.

Previous work of our group showed that Ni supported on monoclinic ZrO$_2$ is a very active catalyst for the CO and CO$_2$ methanation. Considering the two step mechanism, it was proposed that the CO methanation occurs not only on Ni^0 but also on the support [17].

Thereby, this work aims to contribute to the description of the role of oxygen vacancies in the methanation reaction when employing ZrO$_2$ and Ni-based catalyst. This work also identifies the oxygen vacancies via electron paramagnetic resonance (EPR), X-ray diffraction (XRD, reduced *in situ*) and X-ray photoelectron spectroscopy (XPS, reduced *in situ*).

6.2.
Results and discussion

Figure 33 depicts the CO$_2$ conversion and CO and CH$_4$ selectivities versus temperature employing Ni/ZrO$_2$ and NiCa/ZrO$_2$. Both catalysts exhibit very high selectivities to methane (about 99%) and very low towards CO. Furthermore, Ni/CaZrO$_2$ shows higher CO$_2$ conversions when compared with the Ni/ZrO$_2$ catalyst.
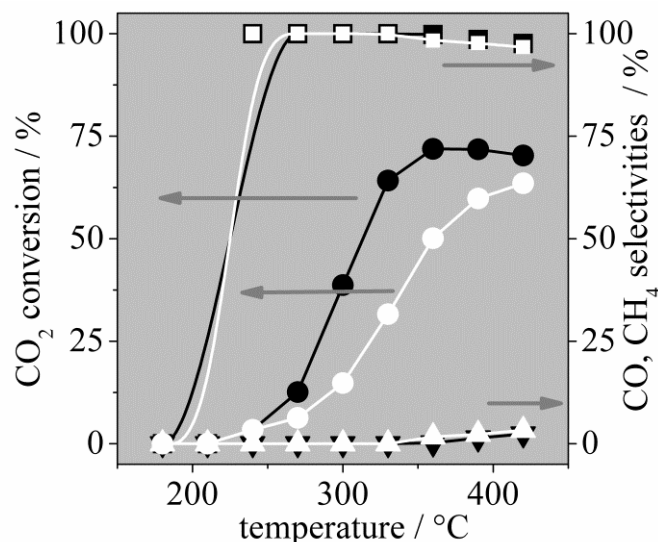
Figure 33. CO_2 conversion (circles), selectivity for CH_4 (squares) and CO (triangles) versus temperature, Ni/ZrO$_2$ (white) and Ni/CaZrO$_2$ (black).

Table 14 depicts the Ni and Ca concentrations of the catalysts and cyclohexane consumption rates. These catalysts exhibit slightly different Ni concentrations and, accordingly, similar cyclohexane dehydrogenation rates. As is well known, these rates are directly proportional to the metallic surface area of the catalysts [52]. Thus, the metallic area values of these catalysts are almost the same. The Ni based catalysts also exhibit the same specific areas. However, when adding Ca to the Ni/ZrO$_2$ catalyst, the CO_2 conversion rate increases around 3 times. This result is in line with the ones of Figure 33.

Table 14. Ni and Ca concentrations, specific area (S), cyclohexane consumption rate (-rC$_6$H$_{12}$), CO_2 consumption rate at 350°C (-rCO$_2$), number of weak strength basic sites (W), medium strength basic sites (M) and strong strength basic sites (St).

	Ni/CaZrO$_2$	Ni/ZrO$_2$
Ni / %wt	5.7	4.8
Ca / %wt	0.7	0
S / m^{2}g^{-1}	69	66
-rC$_6$H$_{12}$ / mmolg h^{-1}	4.0	3.9
-rCO$_2$ /mmol gcat^{-1} min^{-1}	292	110
W (μmol CO$_2$ g^{-1})	48	31
M (μmol CO$_2$ g^{-1})	61	37
St (μmol CO$_2$ g^{-1})	77	70

Figure 34 shows the EPR spectra of the ZrO_2 and $CaZrO_2$ reduced oxides. The ZrO_2 spectrum presents low intensity compared with the one of $CaZrO_2$. Both spectra show broad lines at g = 2.06, which can be assigned to oxygen vacancies and also paramagnetic signals related to Zr^{+3} (g=1.978 and 1.963) [72,73]. The $CaZrO_2$ spectrum also depicts a Fe^{+3} signal at g = 4.3, which might be associated with an impurity of the Ca precursor. The spectra areas were calculated by deconvolution employing Lorentz lines. It was verified that the oxygen vacancies concentration of the $CaZrO_2$ oxide is 1.7 times higher than the one of the ZrO_2 oxide. These samples show two kinds of vacancies: the defects (oxygen vacancies) of the ZrO_2 oxide and the oxygen vacancies which might be generated by the Zr^{4+} replacement by Ca^{2+} in the ZrO_2 monoclinic lattice. Moreover, due to the high intensity of the Ni^0 EPR signal, the spectra of the Ni based catalysts could not be collected [36].
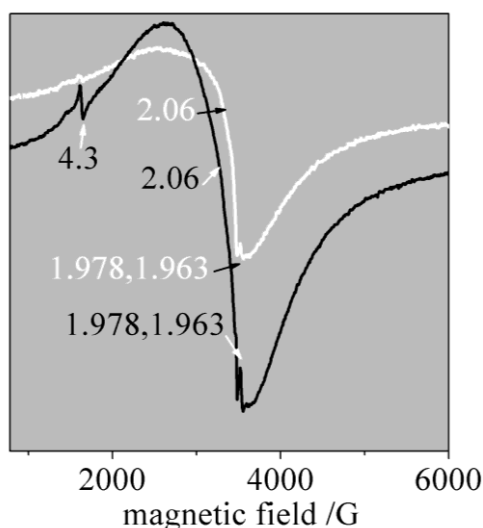
Figure 34. EPR spectrum of ZrO_2 (white) and $CaZrO_2$ (black) supports.

The diffratograms of Ni/ZrO_2 and $Ni/CaZrO_2$ reduced catalysts and the ZrO_2 and $CaZrO_2$ oxides were analyzed by *Rietveld* refinement (Figure 35 and Table 15). All the samples showed about 90-97% of monoclinic ZrO_2 phase along with a small amount of tetragonal ZrO_2 phase, which slightly increases when Ca is in the solid composition. Both the Ni/ZrO_2 and $Ni/CaZrO_2$ catalysts exhibit Ni^0 and NiO, being the metallic phase concentration lower for the Ca based catalyst, showing that Ca hinders the NiO reduction. When Ca is added to the ZrO_2 oxide it

81

can be observed that the Zr^{4+} and O^{2-} occupancy factors decrease, the Ca^{2+} occupancy factor increases and the ZrO_2 monoclinic cell volume increases as well. It is important to mention that this increase in volume was also observed by Drazin et al. [74] . This result is in line with the EPR data suggesting that Ca^{2+} replaces Zr^{4+} in the ZrO_2 monoclinic lattice. However, the EPR spectra of ZrO_2 also show oxygen vacancies whereas this does not occur in the case of the XRD results (see O^{2-} occupancy factors of ZrO_2 monoclinic). It is worth stressing that the EPR measurements were carried out employing reduced samples whereas these oxides were analyzed oxidized by XRD (see methodology).

Comparing the Zr^{4+} and O^{2-} occupancy factors of the ZrO_2 monoclinic lattice of the Ni/ZrO_2 catalyst (reduced) with the ones of ZrO_2 (oxidized), it can be inferred that the former show lower values. Moreover, the ZrO_2 cell volume of the Ni/ZrO_2 catalyst is higher than the one of the ZrO_2 oxide. These changes are related to the Zr^{4+} replacement by Ni^{2+} in the monoclinic lattice and also to the reduction process. Indeed, Ni^{2+} in the ZrO_2 monoclinic lattice of the Ni/ZrO_2 catalyst was also observed by other authors [37,75].

Due to software limitations, the fitting error increases when both Ni^{2+} and Ca^{2+} are introduced in the ZrO_2 lattice. Thus, only Ca^{2+} was considered in the ZrO_2 lattice of the $Ni/CaZrO_2$ catalyst reduced. The same changes described above when comparing ZrO_2 and $CaZrO_2$ parameters can be verified for both Ni catalysts. Thus, it can be inferred that Ca^{2+} (ionic radius 0.114 nm) replaces Zr^{4+} (ionic radius 0.084 nm) in the monoclinic lattice and the amount of this element is much higher than the one of Ni^{2+} observed in the ZrO_2 lattice of the Ni/ZrO_2 catalyst (see Ca^{2+} and Ni^{2+} occupancies).

Table 15. Crystallographic parameters determined by Rietveld Refinement of XRD data.

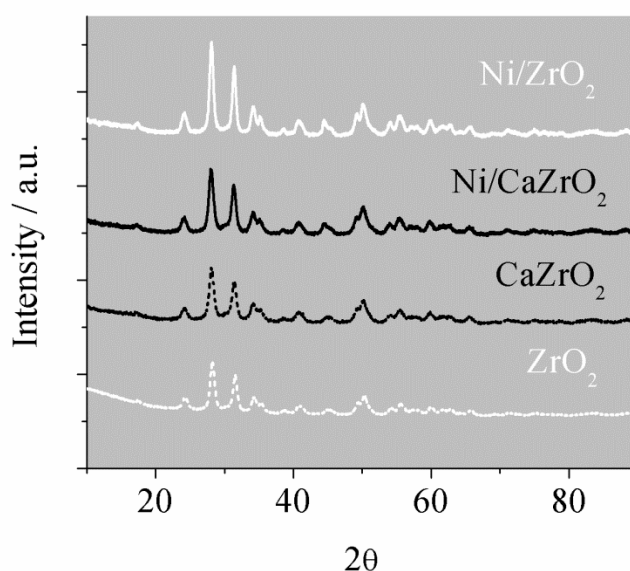| catalysts and supports		Ni/ZrO$_2$	Ni/CaZrO$_2$	ZrO$_2$	CaZrO$_2$
		reduced		oxidized	
MONOCLINIC PHASE (*m*-ZrO$_2$)					
occupancy	1O^{-2}	0.9400	0.9108	1.0000	0.9031
	2O^{-2}	0.9914	0.962	1.0000	0.9477
	Zr^{+4}	0.9910	0.9195	1.0000	0.9146
	Ca^{+2}		0.0805		0.0854
	Ni^{+2}	0.0090			
phase/ wt.%	*m*-ZrO$_2$	92.5400	90.6880	96.9000	95.908
	t-ZrO$_2$	2.0900	3.7750	3.1000	4.0920
	Ni^0	4.1700	1.96800		
	NiO	1.2000	3.5700		
cell volume/ Å^3	*m*-ZrO$_2$	140.2210	140.2624	139.95	140.3976
	t-ZrO$_2$	67.4000	67.0882	67.0000	67.16449
	Ni^0	43.6530	43.4861		
	NiO	55.0000	54.7197		

Figure 35. XRD patterns of the reduced catalyst and oxidized supports.

83

Table 16 displays the Ni2p$_{3/2}$ and Ca2p XPS binding energies of the Ni/ZrO$_2$ and Ni/CaZrO$_2$ reduced catalysts and the species assigned to them. Figure 36 and Figure 37 exhibit the Ni2p$_{3/2}$ and the Ca2p spectra of these catalysts, respectively. Table 16 depicts two Ni2p$_{3/2}$ binding energies being one related to Ni^o and the other to Ni^{2+} into the ZrO$_2$ lattice for both samples. The 860.6 eV band observed in Figure 36 is a satellite.

Table 16 exhibits the Ca2p binding energies of the CaO reference and the reduced Ni/CaZrO$_2$ catalyst. The Ca species binding energies of the Ni/CaZrO$_2$ catalyst decrease around 2.2 eV compared with the CaO ones. This change can be attributed to the insertion of Ca^{2+} into the ZrO$_2$ lattice.

Comparing the Ni^0 amount on the Ni/ZrO$_2$ and NiCa/ZrO$_2$ surfaces (Table 16), it can be observed that the former show higher concentration of this reduced metal. This result is not in line with the cyclohexane dehydrogenation ones which show the same Ni^0 amount on the surface. The sample pretreatment in the case of the XPS analysis and ciclohexane rates employed a gaseous mixture of 5% H$_2$/N$_2$ and pure H$_2$, respectively. When using low H$_2$ concentration (XPS) it is possible to observe that Ca hinders the Ni^{2+} reduction. The XPS results do not show NiO on the surface. Thus, it can also be suggested that Ni^0 is being generated from Ni^{2+} of the ZrO$_2$ lattice [36].

Table 16. Binding energy (BE, eV) and species of Ni2p$_{3/2}$, Ca2p by XPS of the reduced Ni/ZrO$_2$ and Ni/CaZrO$_2$ catalysts.

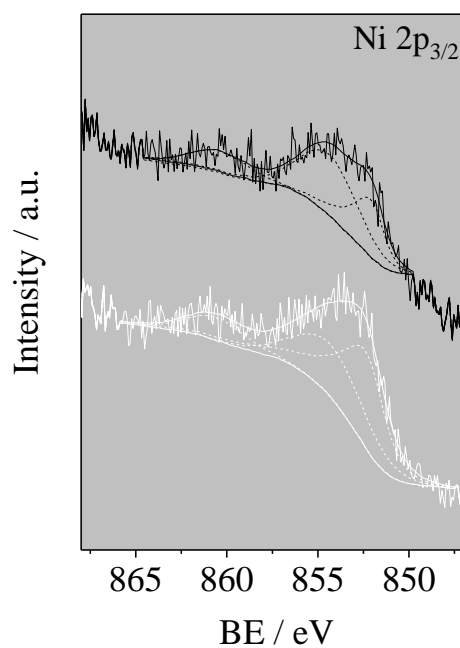| Catalyst	Ni2p$_{3/2}$		Ca2p	
	BE (eV)	species	BE (eV)	species
Ni/ZrO$_2$	852.3 (52%)	Ni^0 [76]		
	854.3 (48%)	Ni^{2+} in the ZrO$_2$ lattice [62]		
Ni/CaZrO$_2$	852.1 (35%)	Ni^0 [76]	344.6 (2p$_{3/2}$)	Ca^{2+} in the ZrO$_2$ lattice
	854.4 (65%)	Ni^{2+} in the ZrO$_2$ lattice [62]	348.1 (2p$_{1/2}$)	Ca^{2+} in the ZrO$_2$ lattice
CaO (reference)			346.8 (2p$_{3/2}$)	CaO
			350.3 (2p$_{1/2}$)	CaO
NiO (reference)	853.3	Pure NiO [50]		

Figure 36. XPS spectra of the Ni $2p_{3/2}$ region of the Ni/ZrO$_2$ (white) and Ni/CaZrO$_2$ (black) catalysts.
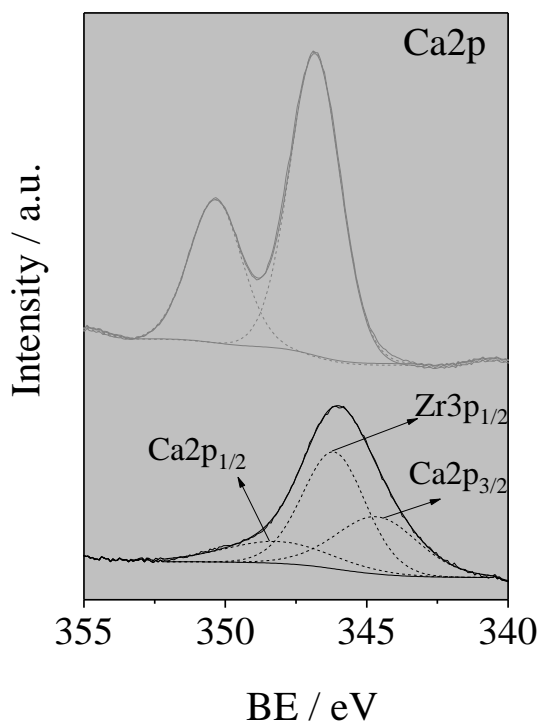

Figure 37. XPS spectra of the Ca2p region of the CaO reference (grey) and Ni/CaZrO$_2$ (black).

The EPR and XRD results show that Ca^{2+} replaces Zr^{4+} in the ZrO_2 lattice whereas the XRD and XPS data reveal that Ni^{2+} substitutes Zr^{4+} in the ZrO_2 lattice of the Ni/ZrO_2 catalyst. Moreover, the XPS analyses show that Ca^{2+} and Ni^{2+} together can replace Zr^{4+} in the ZrO_2 surface. Due to the Ca^{2+}, Ni^{2+} and Zr^{4+}charges, oxygen vacancies are generated in the ZrO_2 lattice. Thereby, pairs of oxygen vacancies and coordinatively unsaturated Zr^{4+} sites (cus) are formed, which are pairs of strong basic-acid sites [76–78]. These results also reveal that the Ca based catalyst show many more pairs of oxygen vacancy-cus than Ni/ZrO_2.
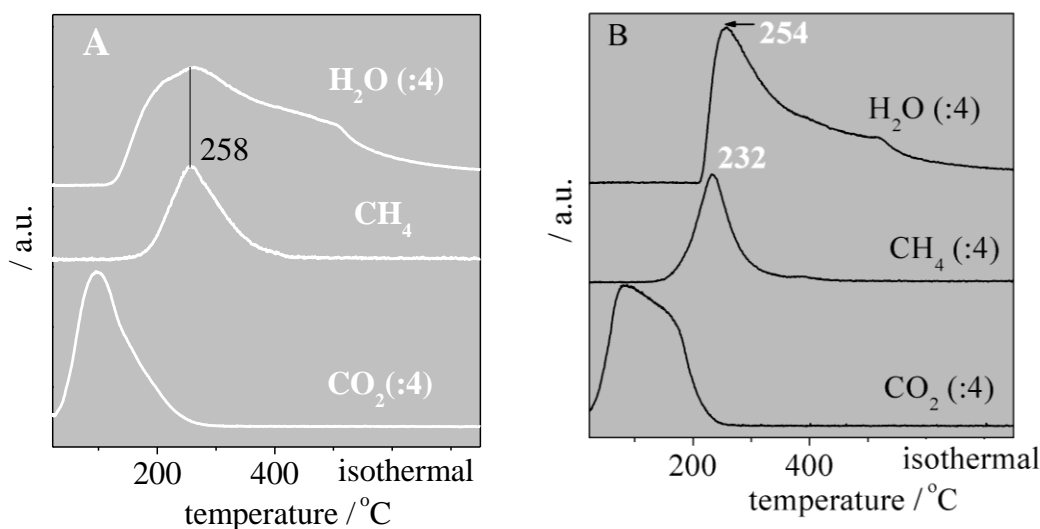
Figure 38. Spectra of the CO_2+H_2 -TPSR over Ni/ZrO_2 (A) and $Ni/CaZrO_2$.

Figure 38A and B depict the CO_2+H_2 - TPSR spectra over Ni/ZrO_2 and $Ni/CaZrO_2$ catalysts, respectively. Both catalysts show CH_4 and H_2O formation and CO_2 desorption. Carbon monoxide is not observed.

Adding Ca to the Ni/ZrO_2 catalyst, the quadruple of CH_4 is generated. These data show that Ca promote, not only the CH_4 synthesis, but also the CO_2 adsorption. Indeed, adding Ca to the Ni/ZrO_2 catalyst there are many more sites for adsorption and transformation of CO_2 into CH_4. Taking the CH_4 bands maxima into account, the $Ni/CaZrO_2$ sites are intrinsically slightly more active than the Ni/ZrO_2 ones. The H_2O spectra of both catalysts show the same maximum (~254°C). However, they exhibit very different shapes and intensities. This behavior can be associate with different reducibility of ZrO_2 and $CaZrO_2$, for

this catalyst it seems not to be a drawback as observed in the case of the Mg based catalyst.

Table 14 depicts that the total number of basic sites of $Ni/CaZrO_2$ is around 35% higher than the one of the Ni/ZrO_2 catalyst. Considering that the CO_2 adsorption occur on the basic sites, these data seem not be in line with the ones of Figure 38A and B. Indeed, the CO_2 adsorption might also occur on oxygen vacancies due to their strong basicity [78]. As the Ca based catalyst shows higher oxygen vacancies concentration than Ni/ZrO_2, it adsorbs much more CO_2.

The CO bond dissociation of the two proposed mechanisms (see introduction) is considered to be the rate-limiting step by some authors [17,25,70,71]. Taking these pieces of information into account, the TPSR of $CO+H_2$ was carried out employing the Ni/ZrO_2 and $Ni/CaZrO_2$ catalysts (Figure 39).

Figure 39 exhibits the $CO+H_2$ -TPSR of both catalysts. The ratio between the amounts of CH_4 synthesized by the Ca based catalyst and the Ni/ZrO_2 catalyst is 2.3. All CO was adsorbed and converted to CH_4. These data show that Ca promote not only the CH_4 synthesis but also the CO adsorption. As CO is a basic molecule it might be adsorbed on the acid sites (cus). The $Ni/CaZrO_2$ catalyst adsorbs more CO as it shows more cus species than the Ni/ZrO_2 catalyst.

Taking into account that the Ca based catalyst is more active than Ni/ZrO_2 in the CO_2 methanation, the $Ni/CaZrO_2$ catalyst shows higher concentration of oxygen vacancy-cus pairs than Ni/ZrO_2 and also the C-O bond dissociation is the rate-limiting step of both mechanisms described above [17,25], it can be suggested that the CO dissociation mainly occurs on these pairs. Thus, the higher the concentration of oxygen vacancy-cus pairs on the catalyst surface, the more active the catalyst is.
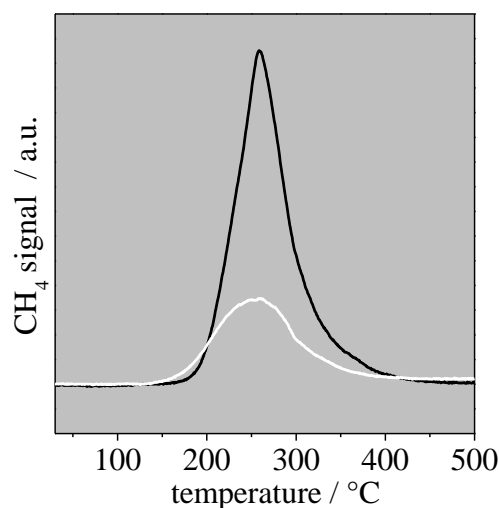
Figure 39. Methane spectra of the CO+H_2 -TPSR over Ni/ZrO_2 (white) and Ni/CaZrO_2 (black) catalysts.

Two CO_2 methanation mechanisms have been proposed. The first one is related to the RWGS followed by the CO methanation. Considering the oxygen vacancy-cus pairs role in the methanation reaction, this mechanism might be described as following: firstly, CO_2 is dissociated on an oxygen vacancy of the support generating CO and adding O to the vacancy; after that, CO is also dissociated on the oxygen vacancy and cus pairs of the support, adding oxygen to the vacancy; next, H_2 is dissociated on the metal and migrates to the support; then, C is hydrogenated to CH_4; finally, H reacts with the O of the lattice recovering the vacancies and generating H_2O.

The second mechanism [25] can be described according the following steps: firstly, CO_2 is adsorbed on the support generating carbonate species; then, hydrogen is dissociated on the metal surface and migrates to the support; next, the carbonate species are hydrogenated to formates; after that, oxygen vacancies promote the C-O bond dissociation of the formates species synthesizing methoxide species; finally, these species undergo hydrogenolysis forming CH_4. According to Wang et al, [25] the rate-limiting step is the formate dissociation to methoxide species. Thus, oxygen vacancies and cus pairs promote the CO dissociation of both mechanisms.

It is also interesting to observe that $Ni/CaZrO_2$ shows more basic sites than $Ni/Mg(Al)O$ and Ni/ZrO_2 (CO_2-TPD) this property might also contribute to the CO_2 adsorption and performance of these catalysts. It is well described in the literature that Ni is an active metal for the CO_2 methanation. Thus, it should also contribute for the activity of these catalytic systems. Furthermore, the Ni^o most important function should be the H_2 dissociation as described before. Once again, ZrO_2 shows an important role in the CO_2 methanation since this oxide promotes the H spillover from the Ni^o phase to the support [79].

6.3.
Conclusion to chapter 6

Adding Ca to Ni/ZrO_2, the metallic surface area did not change whereas the CO_2 consumption rate of the methanation reaction almost tripled. The XRD, XPS and EPR analyses showed that Ca^{2+} but also some Ni^{2+} are in the ZrO_2 lattice surface of the $Ni/CaZrO_2$ catalyst. These cations form oxygen vacancies and unsaturated coordination sites (cus) pairs, which are strong basic and acid sites pairs. In short, increasing the concentration of these pairs by adding Ca to Ni/ZrO_2 not only does the amount of CO_2 adsorbed increase but also the number of active sites of the rate limiting step is enhanced leading to an increase of the Zr based catalyst activity in the methanation of CO_2.

7.
Final conclusion

The supports of the CO_2 methanation catalysts play a major role in the transformation of CO_2 into CH_4. The selectivity and activity are linked to physical-chemical properties of the support. The pair oxygen vacancy – cus, which are strong basic and acid sites, are very relevant for the slowest step of this reaction, i.e., the C-O rupture. It was also verified that the reducibility and basicity of the supports can be important. This work shows that it is possible to create more active and selective catalysts by promoting the cations insertion into the monoclinic ZrO_2 lattice, i. e., generating more pairs oxygen vacancies- cus.

8.
Suggestions for future works

1. To employ other dopants with similar ionic radius from that of the Zr and ensuring a difference in the balance charge of the oxidation state such as: Y^{3+}, Sn^{2+}, Cd^{2+}, Sr^{2+}.

2. To employ DFT (Density functional theory) in order to verify the participation of the pair oxygen vacancies-cus in the rupture of CO bond. As well as to evaluate the two mechanism proposed in the literature.

3. To employ operando spectroscopy (IR, XAS, NAP-XPS) techniques to study the intermediates involved in the reaction.

9.
References

[1] Goeppert A, Prakash GKS, Olah GA. Recycling of carbon dioxide to methanol and derived products; closing the loop. **Chemical Society Reviews**, 2014;43:p. 7995–8048.

[2] Aldana PAU, Ocampo F, Kobl K, Louis B, Thibault-starzyk F, Daturi M, et al. Catalytic CO2 valorization into CH4 on Ni-based ceria-zirconia . Reaction mechanism by operando IR spectroscopy. **Catalysis Today**, 2013;215:p. 201–7.

[3] Tropschuh PF and EP. : Balancing Business and Environmental Concerns, in Sustainable Automotive Technologies. **Springer International**, 2013:p. 185–90.

[4] Association WVC. available at: https://www.wvcoal.com/research-development/audi-is-using-renewable-energy-to-convert-co2-into-methane, accessed on: September; 2018. **West Virginia Coal Association**, n.d.:p. 1–5.

[5] Gao J, Jia C, Li J, Zhang M. Ni/Al2O 3 catalysts for CO methanation : Effect of Al 2 O 3 supports calcined at different temperatures. **Journal of Energy Chemistry**, 2013;22:p. 919–27.

[6] Almeida J De, Lucena Y. Wind energy in Brazil : an overview and perspectives under the triple bottom line 2019;3:p. 69–84.

[7] Resenha Energética Brasileira, Secretaria de Planejamento e Desenvolvimento Energético, Departamento de Informações e Estudos Energéticos. **Ministério de Minas E Energia**, 2018.

[8] UOL. available at: https://www.uol/economia/especiais/energia, accessed on: September; 2018. **Economia**, n.d.:p. 1–3.

[9] Granitsiotis G. Methanation of Carbon Dioxide. **TUDelft**, 2017:p. 1–86.

[10] Bartholomew CH. Carbon Deposition in Steam Reforming and Methanation. **Catalysis Reviews**, 1982;24:p. 67–112.

[11] Cheng C, Shen D, Xiao R, Wu C. Methanation of syngas (H2/CO) over the different Ni-based catalysts. **Fuel**, 2017;189:p. 419–27.

[12] Gao J, Wang Y, Ping Y, Hu D, Xu G, Gu F, et al. A thermodynamic analysis of methanation reactions of carbon oxides for the

production of synthetic natural gas. **RSC Advances**, 2012;2:p. 2358–68.

[13] Nikoo MK, Amin NAS. Thermodynamic analysis of carbon dioxide reforming of methane in view of solid carbon formation. **Fuel Processing Technology**, 2011;92:p. 678–91.

[14] B. Wang, G. Ding, Y. Shang, J. Lv, H. Wang, E. Wang ZL, X. Ma SQ and QS. No Title. **Appl Catal**, 2012;431–432:p. 144–150.

[15] Leal AMM, Blunt MJ, Laforce TC. Advances in Water Resources A robust and efficient numerical method for multiphase equilibrium calculations : Application to CO 2 – brine – rock systems at high temperatures , pressures and salinities. **Advances in Water Resources**, 2013;62:p. 409–30.

[16] Kiewidt L, Thöming J. Predicting optimal temperature profiles in single-stage fi xed-bed reactors for CO2 -methanation. **Chemical Engineering Science**, 2015;132:p. 59–71.

[17] Gao J, Liu Q, Gu F, Liu B, Zhong Z, Su F. Recent advances in methanation catalysts for the production of synthetic natural gas. **RSC Advances**, 2015;5:p. 22759–76.

[18] Vannice MA. The Catalytic Synthesis of Hydrocarbons from H2/CO Mixtures over the Group VIII Metals. **Journal of Catalysis**, 1975;461:p. 449–61.

[19] Ma S, Tan Y, Hang Y, Huo. Methanation of syngas over coral reef-like Ni/Al2O3 catalysts. **Journal of Natural Gas Chemistry**, 2011;20:p. 435– 440.

[20] Inui T, Hagiwara T, Co P, Sieves- M. Prevention of catalyst deactivation coke formation in the methanation of carbon oxides. **Fuel**, 1982;61:p. 537–41.

[21] Nikolla E, Holewinski A, Schwank J, Linic S. Controlling Carbon Surface Chemistry by Alloying: Carbon Tolerant Reforming Catalyst. **JACS Communications**, 2006;128:p. 11354–11355.

[22] Lu J, Fu B, Kung MC, Xiao G, Elam JW, Kung HH, et al. Coking- and sintering-resistant palladium catalysts achieved through atomic layer deposition. **Science**, 2012;335:p. 1205–1208.

[23] Wang H, Fang Y. Perovskite LaFeO 3 supported bi-metal catalyst for syngas methanation. **Journal of Natural Gas Chemistry**, 2012;21:p. 745–52.

[24] Rahmani S, Rezaei M, Meshkani F. Preparation of highly active nickel catalysts supported on mesoporous. **Journal of Industrial and Engineering Chemistry**, 2014;20:p. 1346–52.

[25] Wang F, He S, Chen H, Wang B, Zheng L, Wei M, et al. Active Site-Dependent Reaction Mechanism over Ru/CeO2 Catalyst toward CO2 Methanation. **Journal of the American Chemical Society**, 2016;138:p. 6298–305.

[26] Aziz MAA, Jalil AA, Triwahyono S, Mukti RR, Taufiq-yap YH, Sazegar MR. Applied Catalysis B : Environmental Highly active Ni-promoted mesostructured silica nanoparticles for CO 2 methanation. **"Applied Catalysis B, Environmental,"** 2014;147:p. 359–68.

[27] Garbarino G, Riani P, Magistri L, Busca G, Civile I, Dicca A. A study of the methanation of carbon dioxide on Ni/Al2O3 catalysts at atmospheric pressure. **International Journal of Hydrogen Energy**, 2014;39:p. 11557–65.

[28] Zhang J, Bai Y, Zhang Q, Wang X, Zhang T, Tan Y, et al. Low-temperature methanation of syngas in slurry phase over Zr-doped Ni/c -Al2O3 catalysts prepared using different methods. **FUEL**, 2014;132:p. 211–8.

[29] da Silva DCD, Letichevsky S, Borges LEP, Appel LG. The Ni/ZrO2 catalyst and the methanation of CO and CO2. **International Journal of Hydrogen Energy**, 2012;7:p. 1–6.

[30] Centi G, Palkovits R. Hydrotalcite based Ni–Fe/(Mg ,Al)Ox catalysts for improved CO dissociation , basicity, and particle. **Catalysis Science & Technology**, 2018.

[31] Baldauf-sommerbauer G, Lux S, Aniser W, Bitschnau B, Letofsky-papst I, Siebenhofer M. Steady-state and controlled heating rate methanation of CO 2 on Ni/MgO in a bench-scale fi xed bed tubular reactor. **Journal of CO2 Utilization**, 2018;23:p. 1–9.

[32] Takano H, Shinomiya H, Izumiya K, Kumagai N. CO2 methanation of Ni catalysts supported on tetragonal ZrO2 doped with Ca2+ and Ni2+ ions. **International Journal of Hydrogen Energy**, 2015;40:p. 8347–55.

[33] Jia X, Zhang X, Rui N, Hu X, Liu C. Structural effect of Ni/ZrO2 catalyst on CO2 methanation with enhanced activity. **Applied Catalysis B: Environmental**, 2019;244:p. 159–69.

[34] Lin J, Ma C, Wang Q, Xu Y, Ma G, Wang J, et al. Enhanced low-temperature performance of CO2 methanation over mesoporous Ni/Al2O3-ZrO2 catalysts. **Applied Catalysis B: Environmental**, 2019;243:p. 262–72.

[35] Ashok J, Ang ML, Kawi S. Enhanced activity of CO2 methanation over Ni/CeO2-ZrO2 catalysts : Influence of preparation methods. **Catalysis Today**, 2017;281:p. 304–11.

[36] Rodrigues MT, Zonetti PC, Alves OC, Sousa-aguiar EF. RWGS reaction employing Ni/Mg(Al,Ni)O − The role of the O vacancies. **Applied Catalysis A, General**, 2017;543:p. 98–103.

[37] Sun F, Yan C, Wang Z, Guo C. Ni/Ce-Zr-O catalyst for high CO2 conversion during reverse water gas shift reaction (RWGS). **International Journal of Hydrogen Energy**, 2015;40:p. 15985–93.

[38] Zonetti PC, Letichevsky S, Gaspar AB, Sousa-aguiar EF, Appel LG.

Applied Catalysis A : General The Ni x Ce 0 . 75 Zr 0 . 25 − x O 2 solid solution and the RWGS 2014;475:p. 48–54.

[39] Luhui W, Hui LIU, Yuan LIU, Ying C, Shuqing Y. Effect of precipitants on Ni-CeO 2 catalysts prepared by a co-precipitation method for the reverse water-gas shift reaction. **Journal of Rare Earths**, 2013;31:p. 969–74.

[40] Lu B, Kawamoto K. Preparation of mesoporous CeO 2 and monodispersed NiO particles in CeO2 , and enhanced selectivity of NiO/CeO2 for reverse water gas shift reaction 2014;53:p. 70–8.

[41] Pan Q, Peng J, Sun T, Wang S, Wang S. Insight into the reaction route of CO2 methanation : Promotion effect of medium basic sites. **Catalysis Communications**, 2014;45:p. 74–8.

[42] Eckle S, Anfang H, Ju R. Reaction Intermediates and Side Products in the Methanation of CO and CO2 over Supported Ru Catalysts in H2-Rich Reformate Gases†. **The Journal of Physical Chemistry C**, 2011:p. 1361–7.

[43] Akamaru S, Shimazaki T, Kubo M, Abe T. Applied Catalysis A : General Density functional theory analysis of methanation reaction of CO2 on Ru nanoparticle supported on TiO2 (1 0 1). **"Applied Catalysis A, General,"** 2014;470:p. 405–11.

[44] Karelovic A, Ruiz P. Improving the Hydrogenation Function of Pd/γ-Al2O3 Catalyst by Rh/γ-Al2O3 Addition in CO2 Methanation at Low Temperature. **ACS Catalysis**, 2013;3.

[45] Karelovic A, Ruiz P. Mechanistic study of low temperature CO2 methanation over Rh/TiO2 catalysts. **Journal of Catalysis**, 2013;301:p. 141–53.

[46] Ren J, Guo H, Yang J, Qin Z, Lin J, Li Z. Insights into the mechanisms of CO2 methanation on Ni (111) surfaces by density functional theory. **Applied Surface Science**, 2015;351:p. 504–16.

[47] Aziz MAA, Jalil AA, Triwahyono S, Sidik SM. Methanation of carbon dioxide on metal-promoted mesostructured silica nanoparticles. **"Applied Catalysis A, General,"** 2014;486:p. 115–22.

[48] Silva-calpa LR, Zonetti PC, Rodrigues CP, Alves OC, Appel LG, Avillez RR De. Chemical The ZnxZr1−x O2−y solid solution on m - ZrO2 : Creating O vacancies and improving the m-ZrO2 redox properties. **Journal of Molecular Catalysis A: Chemical**, 2016;425:p. 166–73.

[49] Santos DCRM, Madeira L PF. The effect of the addition of Y2O3 to Ni/a-Al2O3 catalysts on the autothermal reforming of methane. **Catalysis Today**, 2010;149:p. 401–6.

[50] Wagner CD, Riggs WM, Davis LE, Moulder JF, Muilenberg GE. HANDBOOK OFX-RAY PHOTOELECTRON SPECTROSCOPY. **Eden Prairie, Minn : Physical Electronics Division, Perkin-Elmer**

Corp, 1979:p. 1–190.

[51] Biesinger MC, Payne BP, Grosvenor AP, Lau LWM, Gerson AR, St R, et al. Resolving surface chemical states in XPS analysis of first row transition metals , oxides and hydroxides : Cr , Mn , Fe , Co and Ni. **Applied Surface Science Journal**, 2011;257:p. 2717–30.

[52] Santos DCRM, Madeira L, Passos FB. The effect of the addition of Y2O3 to Ni/a-Al2O3 catalysts on the autothermal reforming of methane. **Catalysis Today**, 2010;149:p. 401–6.

[53] Santos MAFE, Lôbo IP, Da Cruz RS. Synthesis and characterization of novel ZrO2-SiO2 mixed oxides. **Materials Research**, 2014;17:p. 700–7.

[54] Trunschke A. Surface area and pore size determination. **Lecture Series: Heterogeneous Catalysis**, 2015;1:p. 1–51.

[55] Bentaleb F, Marceau E. Microporous and Mesoporous Materials Influence of the textural properties of porous aluminas on the reducibility of Ni/Al2O3 catalysts. **Microporous and Mesoporous Materials**, 2012;156:p. 40–4.

[56] Yu X, Wang N, Chu W, Liu M. Carbon dioxide reforming of methane for syngas production over La-promoted NiMgAl catalysts derived from hydrotalcites. **Chemical Engineering Journal**, 2012;209:p. 623–32.

[57] Guskos N, Papadopoulos GJ, Likodimos V, Patapis S. Photoacoustic , EPR and electrical conductivity investigations of three synthetic mineral pigments : hematite , goethite and magnetite. **Materials Research Bulletin**, 2002;37:p. 1051–61.

[58] Chem JM, Maoz BM, Tirosh E, Sadan B, Popov I, Markovich G. Highly defective MgO nanosheets from colloidal self-assembly †. **Journal of Materials Chemistry**, 2011:p. 9532–7.

[59] Shan W, Luo M, Ying P, Shen W, Li C. Reduction property and catalytic activity of Ce1−XNiXO2 mixed oxide catalysts for CH4 oxidation. **Applied Catalysis A, General**, 2003;246:p. 1–9.

[60] Yisup N, Cao Y, Feng W, Dai W, Fan K. Catalytic oxidation of methane over novel Ce–Ni–O mixed oxide catalysts prepared by oxalate gel-coprecipitation. **Catalysis Letters**, 2005;99:p. 207–13.

[61] Enrique C, Gallego J, Mondragón F, Moreno S, Molina R. High stability of Ce-promoted Ni / Mg – Al catalysts derived from hydrotalcites in dry reforming of methane. **Fuel**, 2010;89:p. 592–603.

[62] Romero-sáez M, Dongil AB, Benito N, Espinoza-gonzález R, Escalona N, Gracia F. CO2 methanation over nickel-ZrO2 catalyst supported on carbon nanotubes : A comparison between two impregnation strategies. **Applied Catalysis B: Environmental**, 2018;237:p. 817–25.

[63] Sun M, Xia J, Wang H, Liu X, Xia Q, Wang Y. An efficient NixZryO catalyst for hydrogenation of bio-derived methyl levulinate to γ-valerolactone in water under low hydrogen pressure. **Applied Catalysis B: Environmental**, 2018;227:p. 488–98.

[64] Umegaki T, Yan J, Zhang X, Shioyama H, Kuriyama N, Xu Q. Hollow Ni–SiO2 nanosphere-catalyzed hydrolytic dehydrogenation of ammonia borane for chemical hydrogen storage. **Journal of Power Sources**, 2009;191:p. 209–16.

[65] Wilkinson SK, Water LGA Van De, Miller B, Simmons MJH, Stitt EH, Watson MJ. Understanding the generation of methanol synthesis and water gas shift activity over copper-based catalysts – A spatially resolved experimental kinetic study using steady and non-steady state operation under CO/CO2/H2 feeds. **Journal of Catalysis**, 2016;337:p. 208–20.

[66] Zhu M, Wachs IE. Iron-Based Catalysts for the High-Temperature Water − Gas Shift (HT- WGS) Reaction : A Review. **ACS Catalysis**, 2016;6:p. 722–32.

[67] Takano H, Kirihata Y, Izumiya K, Kumagai N, Habazaki H, Hashimoto K. Highly active Ni/Y-doped ZrO2 catalysts for CO2 methanation. **Applied Surface Science**, 2015.

[68] Somorjai GA, Williams KJ, Boffa AB, Salmeron M, Bell AT. The kinetics of CO2 hydrogenation on a Rh foil promoted by Titania overlayers. **Catalysis Letters**, 1991;9:p. 415–26.

[69] Guilera J, Morante JR, Andreu T. Economic viability of SNG production from power and CO2. **Energy Conversion and Management**, 2018;162:p. 218–24.

[70] Frontera P, Macario A, Ferraro M, Antonucci P. Supported Catalysts for CO2 Methanation : A Review. **Catalysts**, 2017;7:p. 1–28.

[71] Su X, Xu J, Liang B, Duan H, Hou B, Huang Y. Catalytic carbon dioxide hydrogenation to methane : A review of recent studies. **Journal of Energy Chemistry**, 2016;25:p. 553–65.

[72] Martin O, Martín AJ, Mondelli C, Mitchell S, Segawa TF, Hauert R, et al. Methanol Synthesis Indium Oxide as a Superior Catalyst for Methanol Synthesis by CO2 Hydrogenation. **Angewandte Chemie**, 2016;55:p. 6261–5.

[73] Liu H, Feng L, Zhang X, Xue Q. ESR Characterization of ZrO2 Nanopowder. **The Journal of Physical Chemistry**, 1995;99:p. 332–4.

[74] Drazin JW, Castro RHR. Phase Stability in Calcia-Doped Zirconia Nanocrystals. **Journal of the American Ceramic Society**, 2016;99:p. 1778–85.

[75] Chang J, Ryu JO, Lee MJ, Park S-E, Hong D-Y, Jhung SH. Selective Hydrogenation of 1,3-Butadiene over Supported Nickel

Catalyst Obtained from Nickel-Zirconia Solid Solution. **Bulletin of the Korean Chemical Society**, 2005;26:p. 1512–4.

[76] Zhang M, Zhang J, Wu Y, Pan J, Zhang Q, Tan Y. Insight into the effects of the oxygen species over Ni/ZrO2 catalyst surface on methane reforming with carbon dioxide. **Applied Catalysis B: Environmental**, 2019;244:p. 427–37.

[77] Liu Y, Xia C, Wang Q, Zhang L, Huang A, Ke M, et al. Direct dehydrogenation of isobutane to isobutene over Zn-doped ZrO2 metal oxide heterogeneous catalysts. **Catalysis Science & Technology**, 2018;8:p. 4916–24.

[78] Mcfarland EW, Metiu H. Catalysis by Doped Oxides. **Chemical Reviews**, 2013;113:p. 4391–427.

[79] Rodrigues CP, Zonetti PC, Silva CG, Gaspar AB, Appel LG. Chemicals from ethanol — The acetone one-pot synthesis. **Applied Catalysis A, General**, 2013;458:p. 111–8.